Remote control: the cancer cell-intrinsic mechanisms that dictate systemic inflammation and anti-tumor immunity

Wellenstein, M.D.

Distinct p53 hotspot mutations differentially regulate immunotherapy response in breast cancer through activation of autophagy

Max D. Wellenstein[1], Stefan Prekovic[2, #], Isabel Mayayo-Peralta[2, #], Onno B. Bleijerveld[3], Liesbeth Hoekman[3], Cheei-Sing Hau[1], Kevin Kos[1], Elisabeth A.M. Raeven[1], Kim Vrijland[1], Daphne Kaldenbach[1], Danique E.M. Duits[1], Anni Laine[1], Maarten Altelaar[3, 4], Wilbert Zwart[2, 5], Karin E. de Visser[1, 6, *]

Manuscript in revision

Affiliations
[1] Division of Tumor Biology & Immunology, Oncode Institute, Netherlands Cancer Institute, Amsterdam, The Netherlands; [2] Division of Oncogenomics, Oncode Institute, Netherlands Cancer Institute, Amsterdam, The Netherlands; [3] Proteomics Facility, Netherlands Cancer Institute, Amsterdam, The Netherlands; [4] Biomolecular Mass Spectrometry and Proteomics, Utrecht Institute for Pharmaceutical Sciences, Utrecht University, Utrecht, The Netherlands; [5] Laboratory of Chemical Biology and Institute for Complex Molecular Systems, Department of Biomedical Engineering, Eindhoven University of Technology, Eindhoven, The Netherlands; [6] Department of Immunohematology and Blood Transfusion, Leiden University Medical Center, Leiden, Netherlands.

[#] These authors contributed equally

* Corresponding author

Abstract

TP53 is one of the most frequently mutated genes in breast cancer. While p53 mutations often lead to loss of wild-type p53 activity, they can have a wide variety of gain-of-function (GOF) consequences. The impact of these GOF mutations in p53 on the anti-tumor immune response in breast cancer remains elusive. To address this, we have generated mouse mammary tumor models based on orthotopic injection of isogenic cancer cell lines harboring the p53 mutations that most frequently occur in human breast cancer. By comparing the tumor immune landscape of these models and human breast tumors, we have uncovered that specific p53 point mutants consistently induce an immunologically 'hot' tumor phenotype, characterized by high infiltration of cytotoxic T cells, while other p53 mutations induce a non-T cell inflamed ('cold') microenvironment. In accordance with these high T cell levels, the hot p53 mutant tumors respond better to anti-PD-1 immune checkpoint blockade than cold p53 mutant tumors. By comparing the different p53 mutants in terms of proteome profile, chromatin binding properties and protein complex formation, we have uncovered that T cell-enriched p53 mutants activate autophagy. Disruption of autophagy in an immunologically hot p53 mutant tumor abrogated the response to anti-PD-1 therapy. This work demonstrates that not all p53 mutations shape the immune microenvironment of mammary tumors in a similar fashion, and that response to immune checkpoint blockade is dependent on the type of p53 mutation. These insights may help to tailor immune-modulatory therapies to the genetic makeup of breast cancer.

Introduction

The immune system plays a major role in the progression and therapy response of breast cancer[1]. Immunotherapeutic strategies, aimed at harnessing the immune system against tumors, have been shown to be effective in a subset of breast cancer patients, but the majority of patients fails to respond[2]. Heterogeneity in the composition and activation status of the intratumoral immune influx is one of the aspects that determines the efficacy of immunotherapy in breast cancer[2]. The tumor-intrinsic characteristics that orchestrate the response to immunotherapy in breast cancer however, remain largely elusive.

The histological or molecular subtype of breast cancer is one of the key determinants of immune contexture of tumors. An increased presence of tumor infiltrating lymphocytes (TIL) at time of diagnosis has been reported in HER2$^+$ and triple-negative breast cancer compared to luminal cancers[1,3,4]. In addition, besides breast cancer subtype, there is emerging evidence that aberrantly expressed or mutated genes that drive tumorigenesis can have profound non-cell-autonomous effects on the tumor microenvironment[5]. One such gene is *TP53*, encoding p53, which is one of the most frequently mutated genes in breast cancer[6]. Deletion of this tumor suppressor gene drives proliferation and dissemination of cancer cells[7], but also exerts strong effects on the tumor immune microenvironment. Cancer cell-intrinsic loss of p53 has been shown to drive inflammation in mouse models of colon[8,9], pancreatic[10,11], lung[12], uterine[13], prostate[14] and breast cancer[15].

In human breast cancer, *TP53* is more often mutated than homozygously deleted, and there is a strong enrichment across cancer types of specific mutated residues, termed hotspot mutations[16,17]. The occurrence of these hotspot mutations has led to the hypothesis that there is an evolutionary advantage for the tumor to accumulate specific mutations in *TP53* that do not necessarily lead to loss of gene function (LOF), but rather lead to gain of functions (GOF)[18-20]. Indeed, in cancer cell lines and mouse models, it has been widely shown that introduction of certain mutant forms of p53 can give rise to novel phenotypes compared to the p53-null situation[19-21]. In line with this, systematic assessment of the cellular effect of 10.000 *TP53* mutations showed that a number of these mutations can more potently activate proliferative and survival signaling pathways than p53 loss and as such endow cancer cells with growth advantage[22].

In breast cancer patients, overall survival and response to standard of care therapies is strongly determined by whether tumors express wild-type (WT) or mutated *TP53* [23]. In human breast tumors, immune cell numbers or immune-related gene signatures are altered depending on whether *TP53* is WT or mutated[24,25]. In addition, response to immune checkpoint inhibitors was more favorable in lung cancer patients harboring any p53 mutations compared to p53 WT tumors[26-28]. Although these studies suggest a role for mutant p53 in influencing immune activation in tumors, it remains unknown whether p53 deletion and distinct p53 mutations are functionally equivalent in shaping the immune landscape of breast tumors and the response to immunotherapy.

To address whether specific mutations in p53 can dictate response to immunotherapy, we have generated *in vivo* models of p53 mutant breast cancer, based on orthotopically transplanted cell lines derived from spontaneous tumors of different genetically engineered mouse models (GEMMs). By reintroducing the murine equivalents of p53 hotspot mutations that frequently occur in human breast cancer in p53-null isogenic GEMM-derived cell lines and by examining their respective tumor immune landscapes, we have identified specific p53 mutations that consistently induced a T cell-inflamed (immunologically 'hot') or non-T

cell inflamed (immunologically 'cold') tumor microenvironment. Importantly, T cell-enriched p53 mutant mammary tumors responded better to immune checkpoint blockade than T cell-depleted p53 mutant tumors. We demonstrate that p53 mutants form unique protein complexes, while losing their ability to bind chromatin directly. By assessing the cancer cell proteome by mass spectrometry, we have uncovered that autophagy plays a key role in shaping the tumor immune landscape. We demonstrate that immunologically cold p53 mutants show a reduction in autophagic flux, which leads to reduced cytokine signaling and impaired recruitment of T cell subsets. Disruption of autophagy signaling by silencing the *Atg2a* and *Atg2b* genes in hot p53 mutant cancer cells reduced T cell influx into tumors and abrogated response to immune checkpoint blockade *in vivo*. This study demonstrates that not all p53 mutants are equal in their effect on the tumor immune microenvironment and indicates that screening for specific p53 aberrations in breast cancer may help guide personalized immune intervention strategies.

Results

p53 hotspot mutations induce distinct tumor immune landscapes

Besides having a profound effect on cancer cell-intrinsic signaling, loss of p53 has been described to have non-cell-autonomous effects in tumors, most notably on the immune microenvironment[5]. To examine whether p53 hotspot mutations can have altered immune-modulatory function compared to p53 deletion in breast cancer, we derived cell lines from two GEMMs: the wild-type (WT) p53 *Wap-cre;Cdh1$^{F/F}$;Akt$^{E17K/+}$* (WEA) model for invasive lobular breast carcinoma[29] and of the p53-null *K14-cre;Brca1$^{F/F}$;Trp53$^{F/F}$* (KB1P) model for basal-like breast cancer[30]. In WEA cells, we first used CRISPR/Cas9 to delete endogenous p53, and subsequently re-introduced the murine equivalents of p53 hotspot mutants that are most frequently observed in human breast cancer into both WEA and KB1P cells: R172H, Y217C, G242S, R245W, R270H and R277K (corresponding to human R175H, Y220C, G245S, R248W, R273H and R280K)[31], as well as an empty vector (EV) in the p53-null cells (referred to as 'KO') (**Fig. 4.1a, Extended Data Fig. 4.1a – d**). In addition, we introduced the R246S mutant (corresponding to human R249S), which has limited prevalence in breast cancer (**Extended Data Fig. 4.1b**), but is considered a hotspot mutation in several other cancer types, such as hepatocellular carcinoma[32]. These hotspot mutations are all missense mutations localized in the DNA binding domain of p53. Importantly, expression of mutant p53 transgenes in WEA cells was equivalent to the levels of endogenous WT p53 in the control cell line, excluding potential effects of overexpression of the transgenes (**Extended Data Fig. 4.1d**). *In vitro,* the Y217C and G242S mutant WEA cell lines displayed enhanced growth kinetics, while in KB1P the p53-KO grew fastest (**Extended Data Fig. 4.1e**). We then orthotopically transplanted the p53 mutant WEA and KB1P cells into WT syngeneic mice (**Fig. 4.1a**). *In vivo,* similar tumor growth kinetics were observed for all mutants in both WEA and KB1P (**Extended Data Fig. 4.1f**).

Having established two isogenic GEMM-derived mammary tumor cell line models, each differing in just one mutated residue in the p53 gene, we next analyzed the immune cell contexture of the different p53 mutant tumors by flow cytometry. Comparing the WEA p53-WT and KO tumors showed a marked increase in immune influx in the KO, most notably in the lymphoid arm, as well as macrophages, eosinophils and dendritic cells (DCs) (**Fig. 4.1b, Supplemental Fig. 4.1a**). Interestingly, comparing the relative frequencies of immune

cell subsets in WEA mammary tumors with different p53 mutations revealed distinct groups of overall T cell inflamed ('hot') and non-T cell inflamed ('cold') tumors (**Fig. 4.1b**). While the Y217C and G242S mutant tumors showed an immune composition comparable to p53-null (KO) tumors, the R172H, R245W, R246S, R270H and R277K mutants displayed a reduction of various immune cell populations, most notably in $CD8^+$ and $CD4^+$ T helper (T_H) cells, regulatory T cells (Tregs) and B cells (**Fig. 4.1b**). KB1P tumors also showed marked p53 mutant-specific differences in immune cell frequencies in the tumors. In KB1P tumors, $CD8^+$ T cells, $CD4^+$ T_H cells and B cells were highest in the p53-KO and p53-Y217C groups compared to the other mutants (**Fig. 4.1c**). G242S, which was T cell-enriched in WEA tumors, showed a different immune profile in KB1P tumors, possibly reflecting the additional effect that the molecular subtype may have on mutant-p53-mediated immune influx[25].

We assessed two additional GEMM-derived cell lines, *K14-cre;Cdh1$^{F/F}$;Trp53$^{F/F}$* (KEP) and *K14-cre;Trp53$^{F/F}$* (KP), both transduced with the p53-R172H, Y217C or R277K mutant constructs or empty vector (EV – KO) (**Extended Data Fig. 4.2a**). KP tumors mainly represent mammary carcinomas and carcinosarcomas and KEP tumors represent invasive lobular carcinomas[33]. Analysis of the tumor microenvironment revealed that KEP tumors were consistently T cell-inflamed when containing Y217C mutation or p53 deletion, compared to those with R172H and R277K mutations (**Extended Data Fig. 4.2b, c**). In KP tumors, p53-Y217C tumors were enriched for $CD8^+$ T cells, but relatively low in other T cell subsets and p53-KO tumors were generally low in immune cell content, while the R277K mutant appeared highest in overall immune cell frequencies, suggesting additional mechanisms at play in KP tumors (**Extended Data Fig. 4.2b, c**). Taken together, these data suggest that specific p53 mutations can help establish a hot (KO, Y217C) or cold (R172H, R277K) immune microenvironment, which showed consistent immune phenotypes in 3 out of 4 models assessed.

To determine the relevance of these findings to human breast cancer, we used CIBERSORT[34] to probe the association between the different p53 mutants and immune composition in the Cancer Genome Atlas (TCGA) dataset (**Fig. 4.1a**). Interestingly, T cell subsets such as $CD8^+$ T cells and memory $CD4^+$ T cells were enriched in tumors with homozygous deletion (KO) of p53, as well as the Y220 and R273 mutations, compared to the R175, G245, R248 and R280 mutants (**Fig. 4.1d**). These findings indicate that in human breast cancer and in murine models representing different breast cancer subtypes, there is a consistent immune-enriched phenotype in the murine Y217 (human Y220) mutant and p53-KO, and a consistent immune-depleted phenotype in the R172 (R175), R245 (R248) and R277 (R280) mutants, while the other mutants differ between the datasets. Accordingly, gene set enrichment analysis (GSEA) comparing hot p53-KO and Y220 with cold p53-R175 and R280 human breast tumors further revealed that hot mutants show significant enrichment for genes related to antigen presentation and the adaptive immune response (**Fig. 4.1e**). In addition, focusing on $CD8^+$ T cells in WEA and KB1P murine mammary tumors and human breast cancer in TCGA revealed a significant correlation between intratumoral cytotoxic T cell levels and specific p53 aberrations (**Fig. 4.1f**). These data suggest that T cell-depleted mutants have gained immune-modulatory functions compared to p53-null/Y217C tumors that allow them to repel cytotoxic cells from their environment.

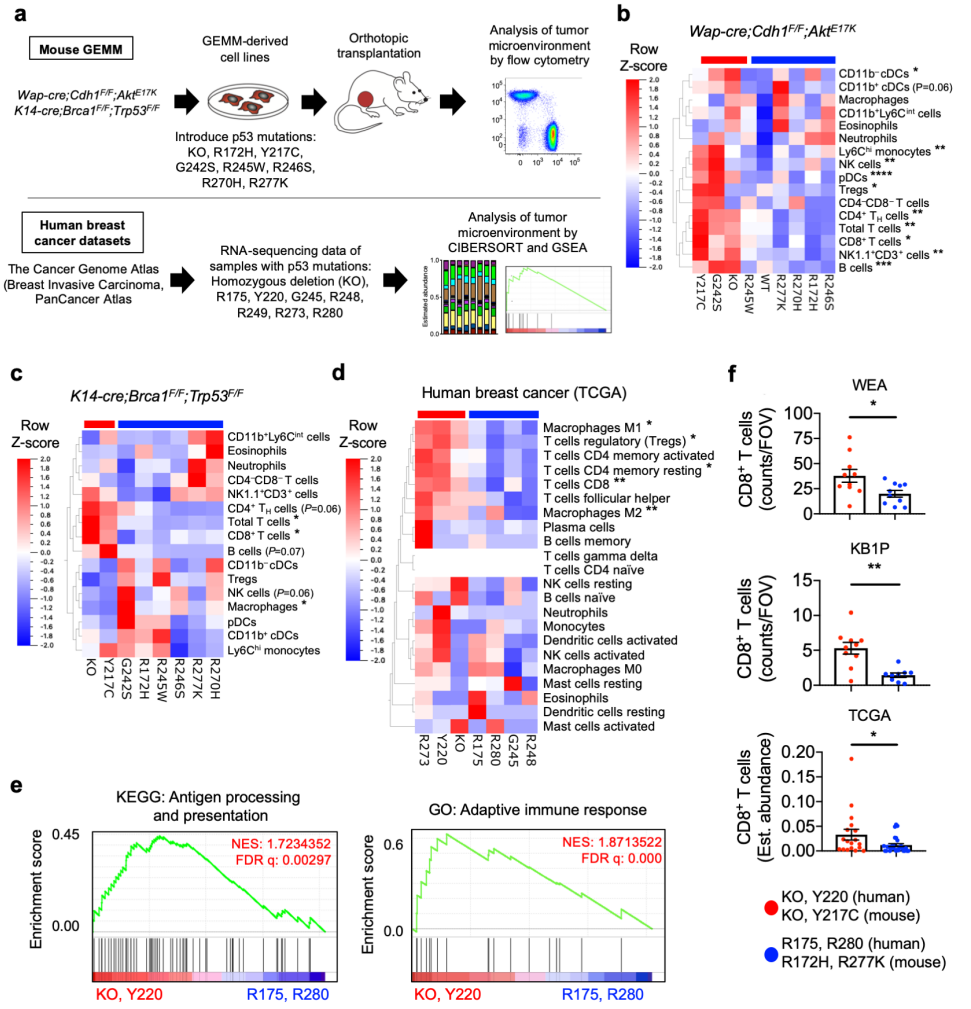

Since we observed striking differences in the composition of the primary tumor microenvironment, we wondered whether the systemic immune milieu might also be altered by the distinct p53 hotspot mutations. We have previously shown that cancer cell-intrinsic loss of p53 activates macrophages to produce IL-1β in primary breast tumors in a WNT-dependent manner, thereby eliciting a systemic inflammatory response driving expansion and activation of metastasis-promoting neutrophils[15]. We therefore assessed systemic neutrophilia in mice bearing WEA p53 mutant tumors and observed that neutrophil levels increase upon KO of p53 compared to p53-WT, and is equally high across the different p53 mutants (**Extended Data Fig. 4.3a, Supplemental Fig. 4.1b**). Accordingly, circulating T cell levels were equally decreased across the p53 mutants and p53-null, compared to p53-WT tumor bearing mice (**Extended Data Fig. 4.3b**). In line with our previous observations[15], bone marrow-derived macrophages (BMDM) cultured with conditioned medium from the different p53 mutant and p53-null WEA cell lines showed equal induction of *Il1b* expression,

Figure 4.1. Hotspot p53 mutations in breast cancer differentially shape the tumor immune landscape. a. Schematic overview of study setup. The immune landscape of isogenic GEMM-cell line tumors expressing p53 mutations are compared to that of human breast tumors to identify p53 mutations that induce similar immune phenotypes. **b.** Heatmap depicting the average frequency of indicated intratumoral immune cells (% of live cells) of the different p53 mutant *Wap-cre;Cdh1$^{F/F}$;Akt^{E17K}* (WEA) tumors at disease end-stage (tumor size ±225 mm^2) as determined by flow cytometry. Based on relative frequency of T cell subsets, mutants are divided into T cell inflamed/'hot' (KO, Y217C, G242S) or non-T cell inflamed/'cold' (R172H, R245W, R246S, R270H, R277K and WT) mutants (n=4–5 mice/group). **c.** Heatmap depicting the average frequency of indicated intratumoral immune cells (% of live cells) of the different p53 mutant *K14-cre;Brca1$^{F/F}$;Trp53$^{F/F}$* (KB1P) tumors at disease end-stage (tumor size ±225 mm^2) as determined by flow cytometry. Based on relative frequency of T cell subsets, mutants are divided into hot (KO, Y217C) or cold (R172H, G242S, R245W, R246S, R270H, R277K) mutants (n=3–5 mice/group). **d.** Heatmap depicted average estimated immune cell composition using CIBERSORT on human breast tumors of TCGA with indicated *TP53* mutations. Based on relative frequency of T cell subsets, mutants are divided into hot (KO (homozygous deletion), Y220, R273) or cold (R175, G245, R248, R280) mutants (n=5–22 tumors/group). **e.** Gene set enrichment analysis (GSEA) comparing KO/Y220 with R175/R280 *TP53* mutant human breast tumors from TCGA on pathways related to antigen presentation (left), adaptive immune response (right), with normalized enrichment score (NES) and false discovery rate (FDR) q-value indicated. **f.** Presence of CD8$^+$ T cells in the commonly T cell-enriched p53 mutants (KO, Y217 (Y220)) and T cell-depleted p53 mutants (R172 (R175), R277 (280)) in WEA and KB1P tumors and human breast tumors (TCGA). CD8$^+$ T cell levels were determined by immunohistochemistry (WEA, KB1P) or CIBERSORT (TCGA). Blue (cold) and red (hot) lines above heatmaps indicate immune status in mouse tumors. Data in **f** shows mean ± s.e.m. Asterisks indicate statistically significant changes. * $P < 0.05$, ** $P < 0.01$, *** $P < 0.001$, **** $P < 0.0001$, as determined by Student's t-test (**b – d**) or Mann-Whitney U test (**f**). Statistical analysis comparing immune populations in heatmaps of **b – d** was made between individual hot (annotated in red) and cold (annotated in blue) mutant tumors as follows: for WEA: KO/Y217C/G242S (hot) vs. R172H/R245W/R246S/R270H/R277K/WT (cold); for KB1P: KO/Y217C (hot) vs. R172H/G242S/R245W/R246S/R270H/R277K (cold), for TCGA: KO/Y220/R273 (hot) vs R175/G245/R248/R280 (cold).

which activates p53-loss-induced systemic inflammation (**Extended Data Fig. 4.3c**). These observations suggest that the pathway that activates neutrophils systemically is equal among the different p53 hotspot mutations. Other systemic immune cell populations also remained largely unaltered among the different p53 mutants (**Extended Data Fig. 4.3d – l**). Together, these findings demonstrate that p53 hotspot mutations mainly affect the immune influx in the tumor microenvironment, while the systemic immune composition is equivalent between p53-null and p53-mutant tumor-bearing mice.

Mutant p53-induced immune states shape response to anti-PD-1 therapy

High T cell influx into tumors correlates with better response to immune checkpoint inhibition in breast cancer[1,35]. Because T cell influx into mammary tumors was associated with specific p53 mutations, we hypothesized that tumors with cold p53 mutations would respond differently to anti-PD-1 immunotherapy than tumors with hot p53 mutations. To test this, we selected the four mutants that showed consistent immune phenotypes between mouse and human tumors; two immune-enriched (KO, Y217C) and two immune-depleted (R172H, R277K). T cells that were present in tumors with these mutations showed high expression levels of inhibitory receptors PD-1 and CTLA4 (**Extended Data Fig. 4.4a, Supplemental Fig. 4.1c**). In tumor-draining axillary lymph nodes, mainly Tregs expressed these immune checkpoint molecules regardless of the p53 mutation (**Extended Data Fig. 4.4b**). T cells obtained from all four p53 mutant tumors had similar capacity to become activated upon exogenous stimulation *ex vivo*, as evidenced by the proliferation marker Ki67 and expression of IFNγ, TNFα and Granzyme B (**Extended Data Fig. 4.4a, b**). We next treated mice bearing

the different p53 mutant tumors twice weekly with anti-PD-1, starting when tumors were ±25 mm^2 and continuing until disease end-stage at 225 mm^2 tumor size (**Fig. 4.2a**). In accordance with their T cell-enriched phenotype, KO and Y217C mammary tumors showed significant response to anti-PD-1 treatment in terms of tumor growth and survival, while the R172H and R277K mutant tumors failed to respond (**Fig. 4.2b, c**). These findings demonstrate that the specific p53 mutation that is present in mammary tumors influences the response to anti-PD-1 immune checkpoint inhibitors.

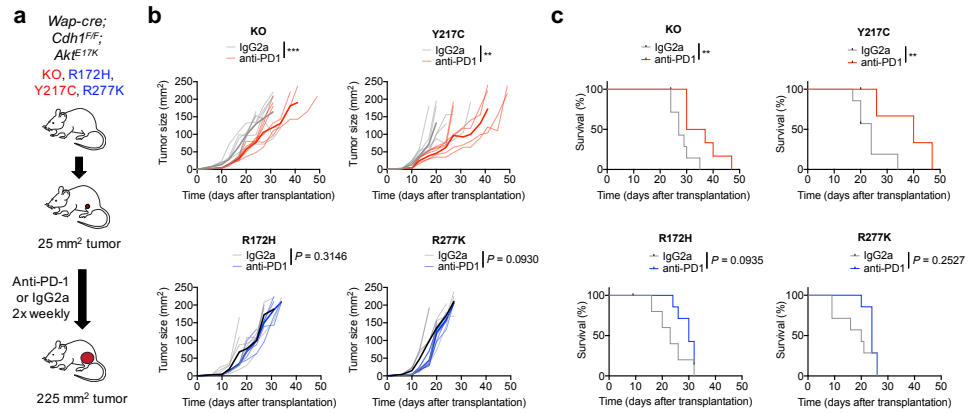

Figure 4.2. Mutant p53-mediated immune landscapes in mammary tumors correlate with response to anti-PD-1 treatment. a. Schematic of anti-PD-1 treatment of mice transplanted with p53-KO, R172H, Y217C and R277K mutant *Wap-cre;Cdh1$^{F/F}$;Akt^{E17K}* (WEA) tumors. Cells are orthotopically transplanted and treatment with anti-PD-1 or IgG2a control antibodies (twice weekly injections of 100 µg) is initiated when tumors are ±25 mm^2 and continued until disease end-stage (tumor size ±225 mm^2). Red (T cell-enriched) and blue (T cell-depleted) indicate immune status of untreated mutant tumors, as determined in Fig. 1. **b.** Tumor growth kinetics in mice with indicated p53 mutations in response to anti-PD-1 or IgG2a treatment (n=8 mice/group). Transparent lines indicate growth curves of individual mice and bold line indicates average growth curve per group. **c.** Kaplan-Meier plot of tumor-specific survival of mice with indicated p53 mutations treated with anti-PD-1 or IgG2a (n=8 mice/group). Exact *P*-values of non-significant changes are indicated. Asterisks indicate statistically significant changes. ** $P < 0.01$, *** $P < 0.001$ as determined by area under the curve (AUC) calculation, followed by Student's t-test (**b**), or log-rank test (**c**).

Mutant p53 forms unique protein complexes

To understand how mutant p53 influences the immune cell influx and response to immune checkpoint inhibition, we next assessed the chromatin binding capabilities and protein complex formation of the different mutant forms of p53. The p53 hotspot mutations assessed here all occur in the DNA binding domain (**Extended Data Fig. 4.1a**).Therefore, we assessed p53 binding to DNA using chromatin immunoprecipitation (ChIP)-sequencing in WEA cells. We observed that WT p53 binds to a variety of chromosomal loci, most dominantly promoters and introns (**Extended Data Fig. 4.5a**). DNA motif analysis revealed mainly binding motifs specific for p53 (**Extended Data Fig. 4.5b**). We next examined chromatin binding by all p53 mutants in WEA cells. While some studies have reported gain of direct DNA binding properties of some p53 mutants[36], others have reported general loss of chromatin binding of most p53 mutants[37]. Consistent with the latter, we found that chromatin binding was lost in all tested p53 mutants, equal to the p53-KO negative control (**Extended Data Fig. 4.5c**).

This shows that in these mammary cancer cell lines, none of the tested p53 mutants directly bind chromatin.

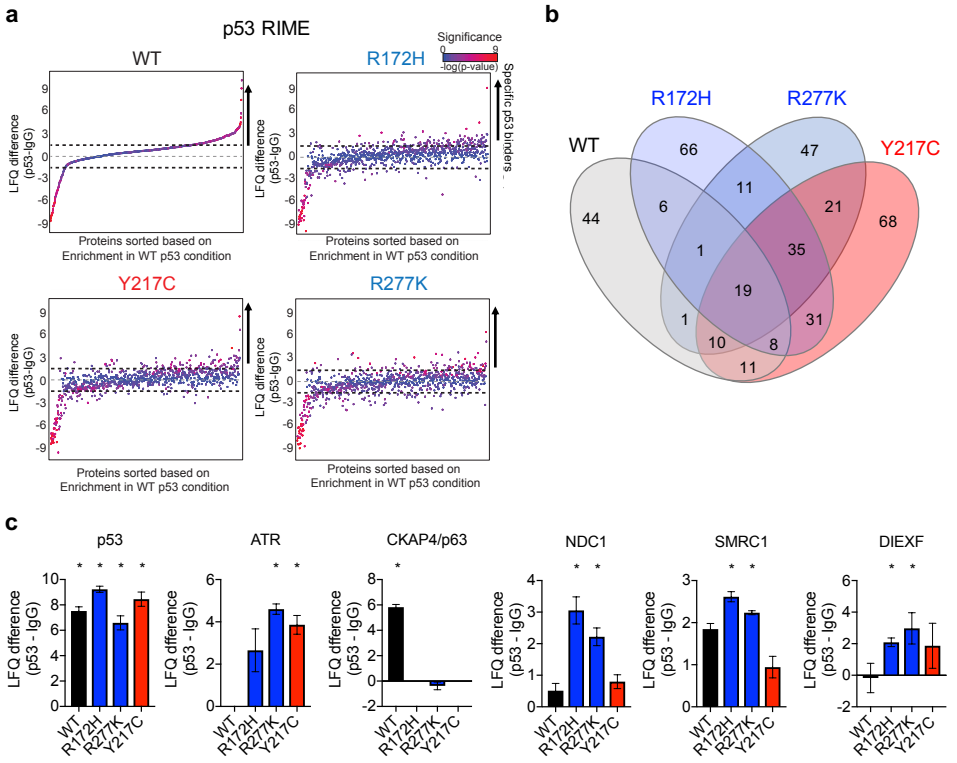

Figure 4.3. p53 mutants form unique protein complexes. a. RIME analysis of proteins interacting with WT or mutant p53, depicted as enrichment of p53-IP over IgG control IP (n=3–4 replicates/group). Proteins above black dotted line (positive label free quantitation (LFQ) difference values) indicate specific p53 binders (indicated by arrow), proteins below black dotted line (negative LFQ difference values) indicate non-p53-specific (background) binders. p53-KO was used as negative control to which all data was normalized. **b.** Venn diagram of p53 interactome showing common and unique binders of WT and mutant p53, normalized to p53-KO. **c.** LFQ differences of selected proteins commonly binding WT and mutant p53 (p53), proteins binding only mutant p53 (ATR) or only WT p53 (CKAP4/p63), and those enriched specifically in cold mutants R172/R277K (n=3–4 replicates/group). Data in **c** show mean ± s.e.m. Asterisks indicate statistically significant changes of enrichment of p53-IP over IgG control IP. * $P < 0.05$, as determined by Student's t-test.

We reasoned that mutant p53 may be binding other co-regulatory factors, which may alter p53 functionality or indirect chromatin binding properties and thus alters gene and protein expression. To test this, we performed rapid immunoprecipitation mass spectrometry of endogenous proteins (RIME)[38] on p53-WT and R172H, Y217C, R277K mutant WEA cell lines, with p53-KO serving as a negative control. We detected numerous p53 interacting proteins in both the p53-WT as well as p53-mutant cells, ranging from 100 to 199 significantly enriched binding partners per group (**Fig. 4.3a**). Using Ingenuity Pathway Analysis to gain insight into the function of these p53 interactors, we observed that WT p53 binds proteins that are involved in transcription and translation, as well as DNA damage signaling and splicing (**Extended Data Fig. 4.5d, Supplemental Table 4.1 – 4**). Proteins involved in these

processes are also bound by mutant forms of p53, but some proteins that WT p53 binds are lost in the p53 mutants (**Fig. 4.3a, b, Extended Data Fig. 4.5e – g**). Comparison of the significantly enriched proteins identified to bind WT or mutant p53 showed proteins unique for each mutant (**Fig. 3b**). For example, we observed that some proteins were interacting with both WT and mutant p53, such as p53 itself, while other proteins were unique to p53 mutants (e.g. ATR) or WT (e.g. CKAP4/p63) (**Fig. 4.3c, Supplemental Table 4.1 – 4**). Examples of highly enriched proteins unique to the cold p53 mutants (R172H and R277K) included nuclear pore complex protein NDC1, chromatin regulating SMRC1 (SMARCC1) and p53 regulator DIEXF (**Fig. 4.3c, Supplemental Table 4.1 – 4**). These data show that rather than directly binding DNA, mutant p53 gains interaction partners, of which a proportion overlaps between p53 mutants and p53-WT, but which also include a set of unique interaction partners per mutation. These unique protein interaction profiles per p53 mutant may potentially form the molecular basis for the observed differences in immune contexture and immunotherapy response between mutants.

Autophagy is activated in immune-enriched p53 mutant tumors

The unique protein complexes formed by mutant forms of p53 may alter protein expression and thereby immune activation. To understand the mechanisms underlying the observed differential immune phenotypes between p53 mutant tumors, we analyzed the proteome of the WEA cell lines using liquid chromatography tandem mass spectrometry (LC-MS/MS). We observed striking differential protein expression patterns comparing p53-WT and p53-KO cells, underscoring the key role of p53 in shaping the overall proteome (**Extended Data Fig. 4.6a, Supplemental Table 4.5**). All p53 mutants showed marked differences compared both to p53-WT and to p53-KO, suggesting potential gain-of-function in protein expression regulation (**Extended Data Fig. 4.6a, Supplemental Table 4.5**). To determine whether these differences in cancer cell proteomes could underlie the immune phenotype we observed, we compared the two consistently hot (KO/Y217C) and two consistently cold (R172H/R277K) p53 mutants (**Fig. 4.4a**). We detected 149 differentially expressed proteins between the cold and hot groups (**Fig. 4.4a, b**). The most significantly overexpressed protein in immune-enriched mutants was ATG2B (**Fig. 4.4b, c**). ATG2B has a crucial role in autophagy, a process that regulates homeostasis under cellular- or nutrient-related stress by breaking down damaged, dysfunctional or redundant cellular components, such as protein aggregates[39]. ATG2 proteins (ATG2A and ATG2B) are essential for autophagy, as silencing of either *Atg2a* or *Atg2b* alone or a combination of both is sufficient to disrupt autophagic flux in mammalian cells[40]. Importantly, reduction of SQSTM1/p62 is a key readout of active autophagy, and we observed significant reduction of this protein in T cell-enriched mutants compared to T cell-depleted mutants, indicating active autophagic flux in immune-enriched mutants (**Extended Data Fig. 4.6b**). Moreover, we observed several proteins that positively regulate autophagy increased (LRP1, FKBP5, SNX7, TOM1, HSP90B) and those that negatively influence autophagy decreased (CUL3) in the immune-enriched mutants compared to the immune-depleted mutants (**Extended Data Fig. 4.6b**).

Because of this differential expression of autophagy-related proteins, we subsequently tested autophagic flux using the GFP-LC3-RFP system[41] in the p53 mutant cell lines. This system allows measurement of the levels of autophagy by determining the rate of GFP-LC3 reduction relative to RFP. Consistent with ATG2B increase and SQSTM1 decrease, we observed a higher autophagic flux in the WEA p53-KO/Y217C mutants compared to

the R172H/R277K mutants (**Fig. 4.4d**). In addition, when assessing autophagic flux in the additional p53 mutant WEA cell lines we see a significant increase in the hot mutants (KO, Y217C and G242S) compared to the cold mutants (R172H, R245W, R246S, R270H and R277K) (**Extended Data Fig. 4.6c, d**). These observations hold true for the p53 mutant KB1P cell lines, in which increased autophagic flux was observed with loss of p53 or Y217C mutation compared to R172H and R277K mutations (**Extended Data Fig. 4.6e**). In human breast cancer, there is an enrichment of genes that positively regulate autophagy in hot (KO and Y220) *TP53* mutant compared to cold (R175 and R280) *TP53* mutant tumors (**Fig. 4.4e**). Together, these data show that activation of autophagy in specific p53 mutant cell lines correlates with an immune-enriched phenotype *in vivo*.

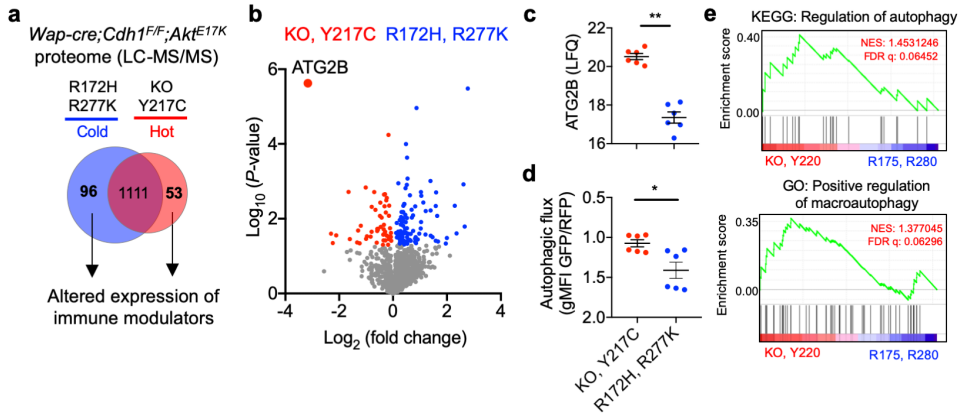

Figure 4.4. T cell-inflamed p53 mutant tumors show activated autophagy. a. Venn diagram of mass spectrometry analysis showing unique and common proteins identified in hot (53 proteins) and cold (96 proteins) mutants, based on all 1260 differentially expressed proteins between any of the mutant p53 and WT p53 *Wap-cre;Cdh1$^{F/F}$;Akt^{E17K}* (WEA) cell lines (see Extended Data Fig. 4.6a) (n=3 replicates/group). **b.** Volcano plot showing commonly differentially expressed proteins between KO/Y217C and R172H/R277K groups. Red circles indicate proteins significantly ($P < 0.05$) up-regulated in hot groups (KO, Y217C), blue circles indicate proteins significantly ($P < 0.05$) up-regulated in cold groups (R172H, R277K) and grey circles indicate non-significantly changed proteins. The highest expressed protein (ATG2B) in hot mutants is indicated. **c.** Abundance (label free quantification, LFQ) of ATG2B protein in WEA cells. **d.** Autophagic flux of indicated mutant p53 WEA cells transduced with autophagy reporter RFP-LC3-GFP and nutrient-starved for 24 hours, as measured by flow cytometry (geometric mean fluorescence intensity (gMFI) of GFP-LC3/RFP-LC3). **e.** Gene set enrichment analysis (GSEA) comparing KO/Y220 with R175/R280 *TP53* mutant human breast tumors from TCGA on pathways related to regulation of autophagy (top) and positive regulation of macroautophagy (bottom), with normalized enrichment score (NES) and false discovery rate (FDR) q-value indicated. Data in **c** and **d** show mean ± s.e.m. Asterisks indicate statistically significant changes. * $P < 0.05$, ** $P < 0.01$, as determined by Mann-Whitney U test.

Cytokine secretion by p53 mutant cancer cells is mediated by autophagy and negatively regulated by mTOR signaling

Aberrations in the p53 pathway can influence immune signaling by alterations in cytokine expression and secretion[5]. We therefore set out to examine whether mutant p53-activated autophagy is involved in cytokine secretion by cancer cells using cytokine arrays on conditioned medium. To test this, we used short hairpin RNAs (shRNAs) to silence expression of *Atg2b* or a combination of *Atg2a* and *Atg2b* in immune-enriched Y217C mutant WEA cells. While *Atg2b* single knockdown was sufficient to significantly decrease autophagic flux,

the double *Atg2a/2b* knockdown proved superior (**Fig. 4.5a**). Compared to non-targeting controls, *Atg2a/2b* silencing reduced secretion levels of several cytokines in the conditioned medium of Y217C mutant WEA cells (**Extended Data Fig. 4.7a, b**). This shows that autophagy contributes to cytokine secretion by $p53^{Y217C}$ cancer cells.

There is an extensive body of literature showing that mTOR signaling negatively regulates autophagy[42] and autophagy-controlled cytokine signaling[43]. Moreover, some mutant forms of p53 have been shown to activate mTOR *in vitro*[44]. Therefore, we next tested the link between hot and cold p53 mutations, autophagy, mTOR and cytokine production in our system. We observed that p53 mutant WEA cells with T cell-depleted phenotypes have an overall higher level of phosphorylated S6 than immune-enriched mutants, indicating active mTOR signaling *in vitro* (**Extended Data Fig. 4.7c, d**). In addition, *in vivo* phospho-S6 levels were increased in cold WEA and KB1P p53 mutant tumors compared to hot p53 mutant tumors (**Extended Data Fig. 4.7e**). Treatment of the cold R172H mutant WEA and KB1P cells with mTOR inhibitor AZD8055 strongly induces autophagy *in vitro* (**Extended Data Fig. 4.7f, g**), suggesting that activated mTOR signaling in immune-depleted mutants negatively influences autophagy. Interestingly, AZD8055-mediated inhibition of the mTOR signaling pathway in p53-R172H WEA cells increases the secretion of cytokines (**Extended Data Fig. 4.7h, i**). Together, these data show that disrupting autophagy in the T cell-enriched Y217C mutant reduces cytokine secretion to levels of T cell-depleted R172H mutant cells (**Extended Data Fig. 4.7j**), which can be reversed by mTOR inhibition. This implies that activated autophagy, which is negatively regulated by mTOR in cold p53 mutants, regulates cytokine secretion by cancer cells and thus potentially regulates immune cell recruitment.

Autophagy is required for response of immune-enriched tumors to anti-PD-1

Next, we tested the impact of autophagy disruption on the intratumoral immune cell influx *in vivo* and its consequences for immunotherapy response. To this end, we orthotopically transplanted Y217C-shControl and Y217C-shAtg2a/2b WEA cells into mammary glands of syngeneic mice. Disruption of autophagy affected primary tumor growth kinetics slightly, but not significantly (**Fig. 4.5b**). At disease end-stage, we observed a modest but significant reduction in total T cell levels, mainly attributed to the $CD4^+$ T helper cells (**Fig. 4.5c**). In addition, $CD11b^-$ cDCs, $CD4^-CD8^-$ T cells and neutrophils were decreased in frequency in *Atg2a/2b* knockdown tumors compared to controls (**Extended Data Fig. 4.8a**). In addition, there was a significantly higher level of cytotoxic Granzyme B-expressing cells in shControl tumors than shAtg2a/2b tumors (**Fig. 4.5d, Extended Data Fig. 4.8b**).

We subsequently tested whether these autophagy-dependent changes had any consequences for the response to anti-PD-1 treatment. We orthotopically transplanted shControl and shAtg2a/b lines and initiated treatment when tumors were 25 mm^2. Similar to the parental Y217C tumors (**Fig. 4.2b, c**), Y217C-shControl responded to anti-PD-1 in terms of tumor growth (**Fig. 4.5e**). Silencing of *Atg2a/2b* led to a significantly impaired response to anti-PD-1 treatment (**Fig. 4.5e**). No significant differences in Granzyme B^+, $CD8^+$ and $CD4^+$ cell levels were observed between the shAtg2a/b and shControl tumors treated with anti-PD-1 (**Extended Data Fig. 4.8b**). Nonetheless, mice treated with anti-PD-1 showed an increase in necrotic tumor tissue in shControl tumors, but not in shAtg2a/2b tumors (**Fig. 4.5f, Extended Data Fig. 4.8b**). In accordance with the differential response of tumor growth kinetics (**Fig. 4.5e**), tumor-specific survival of mice bearing shControl tumors was significantly improved by anti-PD-1 treatment, while silencing of Atg2a/2b abrogated this response (**Fig. 4.5g**).

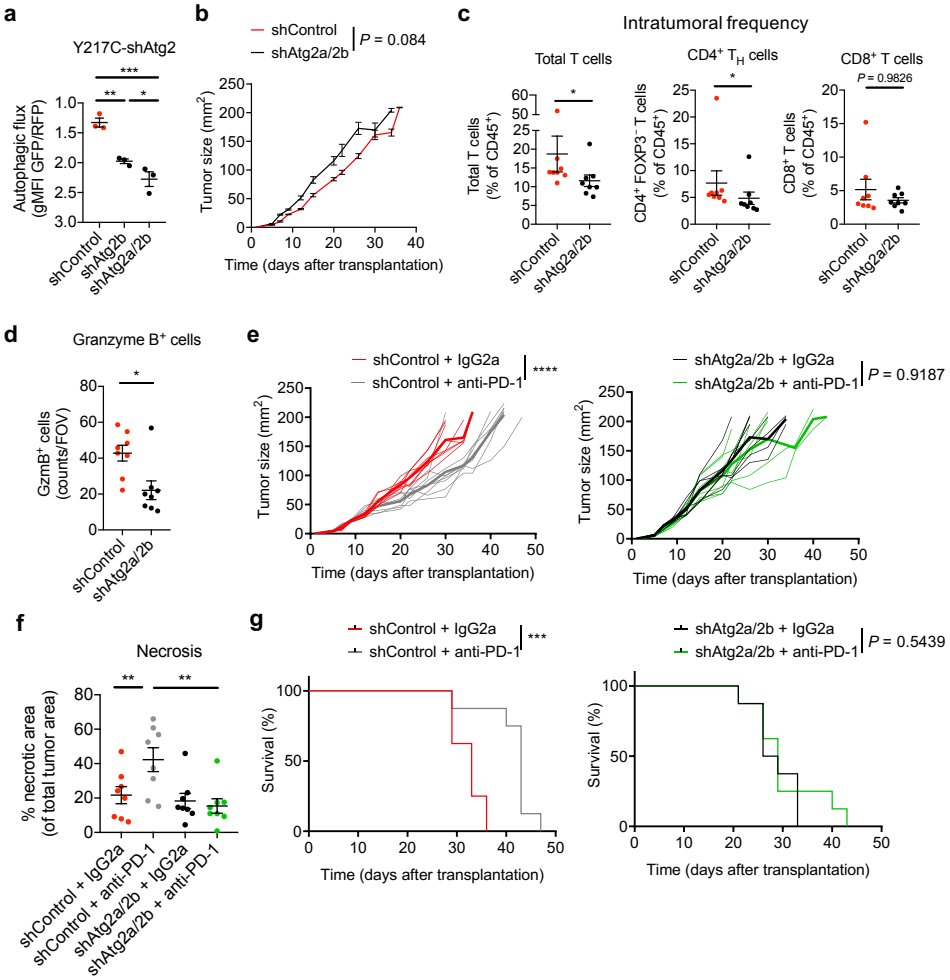

Figure 4.5. Disruption of autophagy partly reverses immune cell influx into p53^{Y217C} tumors and impairs response to immunotherapy. a. Autophagic flux of *Wap-cre;Cdh1$^{F/F}$;Akt^{E17K}* (WEA) cell lines expressing RFP-LC3-GFP that are transduced with shRNAs against *Atg2b,* a combination of *Atg2a* and *Atg2b* (*Atg2a/2b*), or non-targeting controls (n=3 replicates/group). **b.** *In vivo* growth kinetics of WEAP^{Y217C} shControl and shAtg2a/2b tumors (n=8 mice/group). **c.** Frequency (% of live CD45$^+$ cells) of total T cells (all CD3$^+$ cells), CD8$^+$ T cells and CD4$^+$ FOXP3$^-$ T helper (T_H) cells in shControl and shAtg2a/2b tumors at disease end-stage (tumor size ±225 mm^2) (n=8 mice/group). **d.** Number of Granzyme B$^+$ cells per field of view (FOV) in shControl and shAtg2a/2b tumors, as determined by immunohistochemistry (n=8 mice/group). **e.** Growth kinetics of shControl and shAtg2a/2b tumors treated with anti-PD-1 or IgG2a antibodies (twice weekly 100 µg per injection, starting at tumor size 25 mm^2 until ±225 mm^2) (n=8mice /group). Transparent lines indicate growth curves of individual mice and bold line indicates average growth curve per group. **f.** Necrotic area (% of total tumor area) in end-stage shControl and shAtg2a/2b tumors, treated with anti-PD-1 or IgG2a antibody. **g.** Kaplan-Meier plot of tumor-specific survival of mice bearing shControl or shAtg2a/2b tumors treated with anti-PD-1 or IgG2a control antibodies (n=8 mice/group). Exact *P*-values of non-significant changes are indicated. Asterisks indicate statistically significant changes. Data in **a, b, c, d** and **g** show mean ± s.e.m. Asterisks indicate statistically significant changes. * $P < 0.05$, ** $P < 0.01$, *** $P < 0.001$, **** $P < 0.0001$, as determined by one-way ANOVA (**a**), area under the curve (AUC) calculation, followed by Student's t-test (**b, e**), Mann-Whitney U test (**c, d, g**) and log-rank test (**f**).

Together, these data show that autophagy, as induced by specific p53 mutations, is required for the anti-tumor efficacy of immunotherapies in murine breast cancer models.

Discussion

The composition and functional orientation of breast cancer-associated immune cells influence disease outcome and response to treatment, while also providing opportunities for immune-based therapies[2]. Because the quality and quantity of immune influx can vary considerably between patients, we here set out to determine how different genetic aberrations in p53 influence the heterogeneity in immune composition of breast tumors and how this affects immunotherapy efficacy. Comparing the immune microenvironment of tumors harboring the most commonly observed p53 mutations, assessing their proteomic profiles and interaction partners, and linking these observations to human breast cancer, we have uncovered that mammary tumors with loss of p53 or Y217C mutation have an immunologically hot phenotype compared to tumors harboring other p53 mutations, such as R172H and R277K. Moreover, we showed that immune status is linked to autophagy signaling, and that p53 mutant tumors with an immunologically hot phenotype respond better to anti-PD-1 treatment than cold p53 mutants in an autophagy-dependent manner.

The function of p53 in cancer is highly diverse[7], and the function of mutant p53 perhaps even more so[19]. It was proposed several decades ago that mutant p53 can endow cells with novel functions, rather than just leading to loss of gene function[20,45]. Regarding immune activation by p53 mutant tumors, it has been reported in a variety of murine cancer models that some p53 mutations, such as R172H and R248W, can activate immune regulatory pathways such as NF-kB signaling[46-48] and JAK-STAT signaling[10,49], as well as suppress STING signaling[50], thus influencing cytokine production, immune cell recruitment and activation of immunity in the tumor microenvironment. Human breast tumors harboring mutations in p53 generally show a more immune-enriched phenotype than those that are p53-proficient[24], which is dependent on molecular subtype[25]. We here show that not all hotspot mutations in p53 elicit the same effect in terms of immune cell recruitment, but that the composition of the tumor immune microenvironment and response to anti-PD-1 treatment are distinct based on the specific amino acid that is mutated (**Fig. 4.1b – f, Fig. 4.2b, c**). We observed that the p53-KO and Y217C mutant showed consistent T cell-enrichment in 3 out of 4 mouse models and human breast tumors, while the R172H and R277K mutants showed consistent T cell-depletion across datasets (**Fig. 4.1b – f**). The R245W and R246S mutations generally induced an immune-depleted tumor phenotype across datasets as well, suggesting these mutants also have gain of immune-repelling function compared to p53-null tumors. Some mutations differed in immune phenotype between models or between organisms: the G242S mutant deviated between mouse tumors models, clustering in the immune-enriched group in the WEA model, but not in the KB1P model (**Fig. 4.1b, c**). The R270H mutant in mice showed a relative cold phenotype, while human R273 mutant tumors were immunologically hot (**Fig. 4.1b – e**). In addition, of the four murine models tested, one notable exception in mutant p53-mediated immune phenotype is the KP (**Extended Data Fig. 4.2b, c**). It is as of yet unknown what underlies this deviation of KP tumors from the other models. As our data argue, it may be worthwhile to tailor (immuno)therapeutic strategies for breast cancer to the presence of specific p53 mutations. The clinical utility of this is exemplified by the observation that some studies in lung cancer patients show that tumors with any mutation in *TP53* have higher cytotoxic immune influx and improved response to anti-PD-1 treatment compared to WT

tumors[26,28,51], while others report that p53 mutant lung cancer patients respond worse to anti-PD-1 than those with p53 WT tumors[52]. Although there may be a variety of explanations for this, it would be of interest to separate these patients based on specific *TP53* mutations and examine response to see if specific p53 mutational status could be an interesting biomarker for patient stratification in immune-based therapies for breast cancer.

Grouping p53 mutants based on immune phenotypes shows correlation with autophagy activation in mouse and human breast cancer (**Fig. 4.4b – e, Extended Data Fig. 4.6b – e**). There is a well-established link between autophagy and p53 status in cancer cells[53,54]. WT p53 suppresses autophagy[53] and conversely, autophagy is required for degradation of the p53 protein aggregates that form in cells as a result of p53 mutations[55]. p53 status also dictates the influence of autophagy on tumor development. In a mouse model for pancreatic cancer, comparing tumor formation in autophagy-deficient and -proficient mice, it was shown that while autophagy-deficiency accelerates cancer development in a p53-null tumor, but not in a p53-WT tumor[56]. In addition, autophagy activation has strong effects on anti-tumor immunity[57]. In breast cancer patients, high levels of autophagy positively correlate with elevated intratumoral $CD8^+$ T cell-to-Treg and $CD8^+$ T cell-to-macrophage ratios[58], as well as increased overall survival[59]. We here show that the influence of mutant p53 on autophagy is dependent on the specific mutation; mammary tumors with p53 mutations that induce reduced autophagy show lack of response to anti-PD-1 treatment, while tumors expressing other p53 mutations with activated autophagy show the opposite (**Fig. 4.5e, g**). Although it is not yet clear how activated autophagy in these p53 mutants leads to the increased response to anti-PD-1 treatment in these models, it has been proposed that autophagy regulates cytokine production and danger signaling[57]. Indeed, we also observe decreased levels of secreted cytokines in *Atg2a/2b*-knockdown cancer cells (**Extended Data Fig. 4.7a, b**). How this functionally links to the increased anti-tumor immunity upon immune checkpoint inhibition remains a subject of future investigations. It may be of interest to examine the role of mTOR as negative regulator of autophagy in cold p53 mutant tumors, as this pathway negatively regulates autophagy and cytokine secretion (**Extended Data Fig. 4.7h – j**). However, since pharmacological targeting of this pathway also directly impacts adaptive and innate immune cell functionality, as for instance illustrated by the use of mTOR inhibitors as immunosuppressants for organ transplant patients[60], this may not be a desirable strategy to enhance anti-tumor immunity in cold p53 mutant tumors. It is of note that *Atg2a/2b* knockdown does not fully turn hot tumors into cold ones in terms of $CD8^+$ T cell influx (**Fig. 4.5c**), suggesting that additional mechanisms besides autophagy may be at play in shaping the tumor immune microenvironment in these models.

By what molecular mechanism mutant p53 regulates the autophagy machinery in our system remains to be established. We observed that all mutant forms of p53 fail to bind chromatin directly, excluding transcriptional regulation through direct interactions with DNA (**Extended Data Fig. 4.5c).** This lack of direct binding of chromatin by mutant p53 is in line with some reports[37], but may differ per cell line and experimental setup, as others have shown that mutant p53 gains chromatin binding sites relative to WT p53 upon stimulation[36]. All p53 hotspot mutations assessed here occur in the DNA binding domain. These p53 mutations have been divided into contact and structural mutations based on how the mutation influences the structure of p53, with both groups showing functional differences[21,61,62]. This distinction however, does not correlate with the observed immune phenotypes, as the human R248 (murine R245), R273 (R270), R280 (R277) mutants are

considered contact mutations, whereas the R175 (R172), Y220 (Y217), G245 (G242) and R249 (R246) mutants are structural mutants[63-65]. Although mutant p53 may bind DNA and alter transcription in a direct fashion in some models, increasing evidence also suggest that p53 mutants indirectly affect transcription by forming novel protein complexes with other transcription factors and co-regulators[19]. Indeed, in our model, rather than direct chromatin binding, mutant p53 interacts with a different set of proteins (**Fig. 4.3a – c**). In line with these findings, gain of protein interactions have been widely reported for several mutant forms of p53 in breast cancer[66]. Nevertheless, it remains as of yet unclear by what specific protein interaction p53 mutations either induce or inhibit autophagy activation. WT p53 suppresses autophagy[53], so the increased protein levels of ATG2B and high levels of autophagy in the p53-KO and Y217C mutant are in line with these observations (**Fig. 4.4b – d**). It is possible that the cold R172H and R277K mutants gain binding partners that induce repressive signals on the autophagy machinery. The immune-depleted mutants may also employ additional mechanisms, for example by loss of interactions with negative regulators of for example mTOR signaling (**Extended Data Fig. 4.7c – e**).

There is a growing realization that immunotherapy of cancer is not a one-size-fits-all treatment, but should be tailored to tumor- and patient-specific characteristics to attain maximum result. Specific p53 mutations may represent an interesting biomarker to guide treatment. Moreover, this work suggests that the mutant p53-dependent differential immune influx and response to immune checkpoint inhibition can be functionally linked with activation of autophagy. Immunotherapy for breast cancer patients may benefit from using combination treatments[67], and induction of autophagy could be a promising candidate. Although systemic autophagy activation may not be a desired option as it plays critical roles in homeostasis of all cell types, there is a plethora of candidate drugs with potential autophagy modulatory effects that warrant further study in the context of immunotherapy[68]. Taken together, these observations demonstrate that there are distinct immune phenotypes for different p53 hotspot mutations that should be considered when using immune-based therapies in breast cancer.

Methods

Mouse studies

All animal experiments were approved by the Animal Ethics Committee of the Netherlands Cancer Institute and performed in accordance with institutional, national and European guidelines for Animal Care and Use. For orthotopic transplantation experiments, cell suspensions ($5x10^5$ cells) were injected into the right 4th mammary fat pad of 8 – 10 weeks old female wild-type (WT) FVB/N mice (Janvier Labs). Cancer cells used in this study were derived from spontaneous tumors of *Wap-cre;Cdh1$^{F/F}$;Akt^{E17K}* (WEA), *K14-cre;Brca1$^{F/F}$;Trp53$^{F/F}$* (KB1P), *K14-cre;Cdh1$^{F/F}$;Trp53$^{F/F}$* (KEP) or *K14-cre;Trp53$^{F/F}$* (KP) mice, for which the generation and characterization has been described[29,30,33]. Mice were monitored twice weekly and perpendicular diameters of mammary tumors were measured twice per week using a caliper. For intervention studies using anti-PD-1 checkpoint inhibition, mice were randomly distributed over the two treatment arms when tumors reached the size of 25 mm^2 and treated twice weekly with 100 µg of anti-PD-1 (1 mg/mL in PBS, clone RMP1-14, BioXCell) or 100 µg IgG2a control antibodies (1 mg/mL in PBS, clone 2A3, BioXCell) until tumors reached end-stage size of 225 mm^2. Tumor measurements and post mortem analyses were performed in a blinded fashion. Mice were kept in individually ventilated cages and food and water were provided *ad libitum*. The maximal permitted disease endpoints were not exceeded in any of the experiments.

Cell culture

GEMM-derived cell lines were generated as previously described[15]. Briefly, tumor material was collected in ice-cold PBS and mechanically chopped using a McIlwain tissue chopper (Mickle Laboratory Engineering). Tumors were incubated for 30 minutes (min) at 37°C in 3 mg/mL collagenase A, 0.1% trypsin and fungizone in DMEM/F12 with 2% fetal calf serum (FCS). Enzyme reactions were stopped by addition of DMEM/2% FCS and suspensions were dispersed through a 40 µm cell strainer. KB1P an KP cells were cultured in DMEM/F12 containing 10% FCS, 100 IU/mL penicillin, 100 mg/mL streptomycin, 5 ng/mL epidermal growth factor (EGF) (Sigma), 5 µg/mL insulin (Life Technologies) and 5 ng/mL cholera toxin (Gentaur) and WEA and KEP cells were cultured in DMEM supplemented with 10% FCS, 100 IU/mL penicillin, 100 mg/mL streptomycin and 2 mM L-glutamine at 37°C/5% CO_2. To ensure relatedness to parental GEMM tumors, polyclonal cells were used at low passage number for all experiments. HEK293T cells that were used to generate retro- and lentivirus were cultured in DMEM supplemented with 10% FCS, 100 IU/mL penicillin, 100 mg/mL streptomycin and 2 mM L-glutamine. *In vitro* cell growth kinetics were analyzed using the IncuCyte System (Essen Bioscience). Cells were seeded in a 96-well plate at 500 cells per well and imaged every 4 hours (h) until 64 h. Differentiation of bone marrow-derived macrophages (BMDMs) and culture in conditioned medium of p53 mutant cell lines was performed as described[69]. All cell lines were routinely tested for mycoplasma contamination and only mycoplasma-negative cells were used.

Gene modification of cell lines

Endogenous p53 was deleted from p53-proficient WEA GEMM-derived cell lines as previously described[15]. Briefly, WEA cells were transfected with lentiCRISPR v2 (provided by F. Zhang, Addgene plasmid #52961)[70] containing a single sgRNA targeting *Trp53* with of the following sequence: 5'-AGTGAAGCCCTCCGAGTGTC-3'. After puromycin-mediated

selection of transfected cells, polyclonal cell lines were used for all subsequent experiments. Genome editing efficiency was confirmed using the Tracking of Indels by Decomposition (TIDE) algorithm as described[71] (http://tide.nki.nl) and western blotting. KB1P, KEP and KP cells were already p53-deficient.

Mutated p53 was re-introduced in cells by using the pCDH-CMV-MCS-PGK-Blast lentiviral vector (provided by R. Mezzadra) with gBlocks of double strand p53 mutant cDNA (Integrated DNA Technologies) cloned into the expression vector as a BamHI-NotI fragment. All vectors were validated by Sanger sequencing. Virus was produced by transfecting HEK293T cells with the expression vector, pPAX packaging vector and VSV-G envelope vector. Virus was harvested at day 4 and 5. Virus was added to cells in titers that allowed WT-level expression of the mutated transgene (for the WEA cell line) and the same amount of virus was used in the KB1P, KEP and KP cell lines to allow equivalent levels of expression. As control, p53-KO cells were transduced with an empty pCDH-CMV-MCS-PGK-Blast vector (EV). After blasticidin-mediated selection of transduced cells, integration of mutated p53 was assessed by isolating genomic DNA using Viagen DirectPCR Lysis reagent (Cell) supplemented with 200 µg/mL proteinase K according to manufacturer instructions, followed by PCR amplification of the p53 locus and Sanger sequencing, which was analyzed using SnapGene software (version 5.1). To determine expression levels of mutant *Trp53* transgenes, RNA was isolated from cells after selection, followed by RT-qPCR (see below).

To silence *Atg2a* and *Atg2b*, short hairpin RNAs (shRNAs) were used in the pLKO.1 vector. Vectors for shRNAs were collected from the mouse TRC library. To allow stable expression of pLKO.1 lentiviral vectors containing shRNAs, virus was produced in HEK293T cells as described above. WEA-p53^{Y217C} cells were transduced with single shRNAs or co-transduced with both shRNAs and subjected to puromycin selection. Knock-down efficiency was determined by RT-qPCR (see below). The sense strand of the hairpin sequence for *Atg2a* and *Atg2b* silencing used in the *in vivo* experiments was as follows: *Atg2a*: 5'-CGAAAGTATCTACAACAGGAT-3', *Atg2b*: 5'-GCTGCACTTGAAATCCGAGTA-3'.

Flow cytometry

Tumor and lymph nodes were collected in ice-cold PBS and blood was collected in tubes containing heparin. Tumors were mechanically chopped using a McIlwain tissue chopper (Mickle Laboratory Engineering). Tumors were digested for 1 h at 37°C in 3 mg/mL collagenase type A (Roche) and 25 µg/mL DNase (Sigma) in serum-free DMEM medium. Enzyme reactions were stopped by addition of cold DMEM/10% FCS and suspensions were dispersed through a 70 µm cell strainer. Tumor-draining lymph nodes (right axillary lymph nodes) were dispersed through a 70 µm cell strainer to generate single cell suspensions. Blood was treated twice with NH_4Cl erythrocyte lysis buffer. Before staining, cell suspensions were subjected to Fc receptor blocking (rat anti-mouse CD16/32, BD Biosciences) for 10 min at 4°C. Cells were stained with conjugated antibodies for 30 min at 4°C in the dark in PBS/0.5% BSA/2 mM EDTA. Zombie Red fixable viability kit (1:800 in PBS, BioLegend) was added to exclude dead cells. For intracellular cytokine staining, single-cell suspensions were stimulated in IMDM containing 8% FCS, 100 IU/mL penicillin, 100 mg/mL streptomycin, 0.5% β-mercaptoethanol, 50 ng/ml PMA, 1 mM ionomycin and Golgi-Plug (1:1000, BD Biosciences) for 3h at 37°C. Surface antigens were stained first, followed by fixation and permeabilization using the Foxp3 Fixation/Permeabilization kit (eBioscience/ThermoFisher) and staining of intracellular proteins. All experiments were performed using a BD LSR II

flow cytometer using Diva software. Data analyses were performed using FlowJo Software (version 9.9.6 and version 10.6.2).

The following antibodies were used in the experiments: anti-FoxP3-AF647 (150D/E4, eBioscience/ThermoFisher, 1:200), anti-Ly6G-AF700 (1A8, BioLegend, 1:200), anti-F4/80-APC-eF780 (BM8, eBioscience/ThermoFisher, 1:200), anti-SiglecF-PE (E50-2440, BD Biosciences, 1:200), anti-NK1.1-PE-Cy7 (PK136, BioLegend, 1:200), anti-CD3-FITC (145-2C11, eBioscience/ThermoFisher, 1:400), anti-CD8a-PerCP-eF710 (46-0081-82, eBioscience/ThermoFisher, 1:400), anti-CD11c-BV421 (HL3, BD Biosciences, 1:200), anti-Ly6C-BV605 (HK1.4, BioLegend, 1:200), anti-CD11b-BV786 (M1/70, BD Biosciences, 1:400), anti-CD45-BUV395 (30-F11, BD Biosciences, 1:200), anti-B220-BUV737 (RA3-6B2, BD Biosciences, 1:400), anti-CD4-BUV805 (GK1.5, BD Biosciences, 1:200), anti-TNFa-AF700 (MP6-XT22, BioLegend, 1:200), anti-CD4-APC-eF780 (RM4-5, eBioscience/ThermoFisher, 1:200), anti-Granzyme B-PE (GB-11, Sanquin, 1:200), anti-CTLA4-PE-Cy7 (UC10-4B9, eBioscience/ThermoFisher, 1:200), anti-Ki67-PerCP-eF710 (SolA15, eBioscience/ThermoFisher, 1:800), anti-IFNγ-eF450 (XMG1.2, eBioscience/ThermoFisher, 1:200), anti-PD-1-BV711 (29F.1A12, BioLegend,1:200), anti-CD8-BUV395 (53-6.7, BD Biosciences, 1:200), anti-CD45-BUV563 (30-F11, BD Biosciences, 1:200), anti-H-2K^{q}-FITC (FVB haplotype MHC-I) (HK114, BioLegend, 1:200).

Human breast cancer analysis

Human breast tumor data were obtained from the Cancer Genome Atlas (TCGA, Breast Invasive Carcinoma, PanCancer Atlas) via cBioPortal[72,73] (http://cbioportal.org). Samples were selected based on availability of DNA-sequencing, copy-number alterations and RNA-sequencing (994/1084 samples) to allow assessment of gene expression in samples for which *TP53* mutation and homozygous deletions ('homdel', indicated as KO) were known. Lollipop plot of mutation prevalence and location in the *TP53* gene was generated using cBioPortal. Immune influx estimates in indicated *TP53* mutant tumors or in tumors with a homozygous deletion (KO) were determined using CIBERSORT[34] (http://cibersort.stanford.edu), running in absolute mode. Gene Set Enrichment Analysis (GSEA) was performed on KO, R175, Y220 and R280 *TP53* mutant tumors using GSEA software[74,75] on gene sets indicated in figures, which were obtained from MSigDB[76] (https://www.gsea-msigdb.org/gsea/index.jsp). Permutations for both GSEA and CIBERSORT was conducted 1000 times to obtain an empirical null distribution.

Liquid Chromatography-Tandem Mass spectrometry (LC-MS/MS)

Frozen pellets of WEA p53-WT, p53-KO and p53-mutant cells (3 replicates per cell line, ±15x10^{6} cells per replicate) were lysed, reduced and alkylated in heated guanidine (GuHCl) lysis buffer as described before[77]. Lysates were diluted to 2 M GuHCl and digested with trypsin (Sigma) (1:100) for 4 h at 37°C, followed by another overnight tryptic digestion (1:50). Digestion was quenched by the addition of TFA (final concentration 1%), after which samples were desalted on a Sep-Pak C18 cartridge (Waters, Massachusetts, USA). Peptides were vacuum dried and stored at -80°C until LC-MS/MS analysis.

Peptides were reconstituted in 2% formic acid and analyzed by nanoLC-MS/MS on an Orbitrap Fusion Tribrid mass spectrometer equipped with an Easy-nLC1000 system (Thermo Scientific). Samples were directly loaded onto the analytical column (ReproSil-Pur 120 C18-AQ, 2.4 µm, 75 µm × 500 mm, packed in-house). Solvent A was 0.1% formic acid/water and

solvent B was 0.1% formic acid/80% acetonitrile. Peptides were eluted from the analytical column at a constant flow of 250 nl/min. For single-run proteome analysis, a 4 h gradient was employed containing a linear increase from 5% to 35% solvent B, followed by a 15 min wash. The mass spectrometer was run in top speed mode with 3 s cycles. Survey scans of peptide precursors from m/z 375-1500 were performed at 120K resolution with a 4 x 105 ion count target. Tandem MS was performed by quadrupole isolation at 1.6 Th, followed by HCD fragmentation with normalized collision energy 31 and ion trap MS2 fragment detection. The MS2 ion count target was set to 104 and the max injection time was set to 100 ms. Only precursors with charge state 2-7 were sampled for MS2. Monoisotopic precursor selection was turned on; the dynamic exclusion duration was set to 60s with a 10 ppm tolerance around the selected precursor and its isotopes.

RAW files were analyzed by Proteome Discoverer (version 2.3.0.523, Thermo Scientific) using standard settings. MS/MS data were searched in Sequest HT against the mouse Swissprot database (release 2019_02). The maximum allowed precursor mass tolerance was 50 ppm and 0.06 Da for fragment ion masses. False discovery rates for peptide and protein identification were set to 1%. Trypsin was chosen as cleavage specificity allowing two missed cleavages. Carbamidomethylation (C) was set as fixed modification, whereas oxidation (M) and protein N-terminal acetylation were set as variable modifications. Peptide spectrum matches (PSM) were filtered for Sequest HT Xcorr score ≥ 1. The Proteome Discoverer output file containing the LFQ abundances was loaded into Perseus (version 1.6.5.0)[78]. Abundances were Log_2-transformed and the proteins were filtered for at least three out of three valid values in one condition. Missing values were replaced by imputation based on the standard settings of Perseus, i.e. a normal distribution using a width of 0.3 and a downshift of 1.8. Differential proteins were determined using a multiple-sample ANOVA with permutation-based False Discovery Rate (FDR) (threshold 1%). Abundances of differential proteins were Z-scored and hierarchical clustering was performed using default settings.

Chromatin Immunoprecipitation (ChIP)-sequencing

Chromatin immunoprecipitation (ChIP)-sequencing was performed as previously described[79]. Duplicate cell lines from the p53 mutants were fixed in 1% formaldehyde, crosslinked and processed for sonication. 5 µg of p53 antibody (1C12, Cell Signaling Technologies) and 50 µL of Protein G magnetic beads (Invitrogen) were used for each ChIP. Eluted DNA was sequenced using the Illumina Hiseq 2500 analyser (using 65 bp reads) and aligned to the *Mus musculus* mm10 reference genome. Reads were filtered based on MAPQ quality (quality ≥ 20) and duplicate reads were removed. Peak calling over input control was performed using MACS 2.0 peak caller using default parameters. Data was visualized using Easeq[80].

Rapid Immunoprecipitation of endogenous proteins (RIME)

RIME experiments were performed as described[38]. The following antibodies were used: anti-p53 (1C12, Cell Signaling Technology) and anti-mouse IgG (sc-2025, Santa Cruz Biotechnology). Tryptic digestion of bead-bound proteins was performed as described previously[81]. LC-MS/MS analysis of the tryptic digests was performed on an Orbitrap Fusion Tribrid mass spectrometer equipped with a Proxeon nLC1000 system (Thermo Scientific). Raw data were analyzed by Proteome Discoverer (PD) (version 2.3.0.523, Thermo Scientific) using standard settings.

MS/MS data were searched against the Swissprot database (released 2018_06)

using Mascot (version 2.6.1, Matrix Science, UK) with *Mus musculus* as taxonomy filter. The maximum allowed precursor mass tolerance was 50 ppm and 0.6 Da for fragment ion masses. Trypsin was chosen as cleavage specificity allowing two missed cleavages. Carbamidomethylation (C) was set as a fixed modification, while oxidation (M) and deamidation (NQ) were used as variable modifications. False discovery rates for peptide and protein identification were set to 1% and as additional filter Mascot peptide ion score > 20 or Sequest HT XCorr>1 was set. The PD output file containing the abundances was loaded into Perseus (version 1.6.1.3)[78] LFQ intensities were $\log_2$-transformed and the proteins were filtered for at least 66% valid values. Missing values were replaced by imputation based on the standard settings of Perseus, i.e. a normal distribution using a width of 0.3 and a downshift of 1.8. Differentially expressed proteins were determined using a t-test (threshold–Log(p-value) ≥ 1.3 and [x/y] ≥ 1 | [x/y] ≤ -1)). p53-KO cells were used as a negative control. Pathway analysis of p53 binding proteins was performed using Ingenuity Pathway Analysis (IPA) software (Qiagen) (version 01.06), for which all statistically significant enriched (P < 0.05) pathways in which directionality could be determined (i.e. with a positive Z-score) are shown, with a maximum of 10 pathways.

Autophagy measurements

To assess autophagic flux in cells, the pMRX-IP-GFP-LC3-RFP reporter vector was used (provided by N. Mizushima, Addgene plasmid #84573)[41]. Retrovirus was made by transfection HEK293T cells with the pMRX-IP-GFP-LC3-RFP and the pCL-ECO vectors. WEA and KB1P p53 mutant cell lines were transduced and cells expressing the construct were selected using puromycin. For *Atg2*-knockdown cell lines puromycin selection was not possible due to the presence of a puromycin resistance cassette in the pLKO.1 vector. Therefore, the assay was performed on unselected cells. Where indicated, cells were treated with 1 μM mTOR inhibitor AZD8055 (Selleck Chemicals) for 24 hours (h) or starved by exposure to EBSS medium for 24 h to induce autophagy. All GFP/RFP ratios were determined in the RFP^+ transduced population.

RNA isolation and quantitative (q)RT-PCR

Total RNA was isolated using the Isolate II RNA Mini Kit (Bioline). RNA quality and concentration were determined using a 2100 Bioanalyzer (Agilent). RNA was converted to cDNA using Maxima First Strand cDNA Synthesis kit (Thermo Scientific). 20 ng cDNA was analyzed using SensiFAST SYBR No-ROX (Bioline) with 500 nM primers using a LightCycler 480 thermocycler (Roche). *Gapdh* was used as housekeeping gene. Fold change in expression was calculated using $2^{-(\Delta Ct.x\ -\ average[\Delta Ct.control])}$. Primer sequences were as follows: *Trp53 forward (FW):* 5'-CTCTCCCCCGCAAAAGAAAAA-3', *Trp53 reverse (RV):* 5'-CGGAACATCTCGAAGCGTTTA-3', *Atg2a FW:* 5'-CCACCTCTGCAAATCGGCA-3', *Atg2a RV:* 5'-CCAGTTGTCCTGATACCTCCA-3', *Atg2b FW:* 5'-GTCCCCTTGGACAAATGGTGT-3', *Atg2b RV:* 5'-GGACGGACAGGGAAATGGA-3', *Gapdh FW:* 5'-AGGTCGGTGTGAACGGATTTG-3', *Gapdh RV:* 5'-TGTAGACCATGTAGTTGAGGTCA-3'.

Cytokine analysis

Conditioned medium (CM) was prepared by seeding indicated cancer cells at equal density in full medium in a 6-well plate. At ±80% confluency, cells were washed once in PBS and serum-free medium was added to the cells in 50% of normal volume. Where indicated, cells

were treated with 1 μM AZD8055 (Selleck Chemicals) or DMSO to block mTOR signaling. After 24 h, CM was harvested, dead cells and debris were removed by centrifugation and cytokines were measured using Proteome Profiler Mouse Cytokine Array Kit, Panel A (R&D Systems) according to manufacturer's instruction. Signal intensity was determined using ImageJ/FIJI (version 2.0.0).

Protein isolation and Western blot

Cells were lysed using RIPA buffer (50 mM Tris-HCl, pH 7.4, 150 mM NaCl, 1% NP40, 0.5% DOC, 0.1% SDS, 2 mM EDTA) supplemented with cOmplete Protease Inhibitors and phosphatase inhibitors (Roche). Protein concentration was quantified using the Rio-Rad Protein Assay (Bio-Rad). Protein lysates were diluted in 4x LDS Sample buffer (Invitrogen) and supplemented with 100mM dithiothreitol (DTT) were incubated at 95°C for 5 min. Equal amounts of protein (30 μg) were separated by SDS-PAGE electrophoresis using Nu-PAGE 4-12% Bis-Tris midi gels (Invitrogen) and transferred onto Trans-Blot® Turbo™ Midi Nitrocellulose membranes (Bio-Rad) using Trans-Blot Turbo Transfer System (Bio-Rad). Membranes were blocked in 10% Western Blot Blocking Reagent (Roche) in TBS for 1 h at room temperature (RT), after which primary antibody in 5% Western Blot Blocking Reagent (Roche) in TBS-T was added and incubated overnight at 4°C. Membranes were washed using TBS-T and subjected to secondary fluorochrome-conjugated antibodies for 1 h at RT and protein was detected using the Odyssey CLx imaging system (LICOR) and processed using Image Studio Lite (version 5.2.5 LI-COR). The following antibodies were used: anti-phospho-S6 ribosomal protein (Ser235/236) (D57.2.2E, Cell Signaling Technology, 1:1000), anti-total S6 ribosomal protein (5G10, Cell Signaling Technology, 1:1000), anti-β-actin (AC-15, Sigma, 1:5000), IRDye 680RD anti-mouse IgG secondary antibody (Li-COR, 1:10000) and IRDye 800CW anti-rabbit IgG secondary antibody (LI-COR, 1:10000).

Immunohistochemistry

Immunohistochemical analyses were performed by the Animal Pathology facility of the Netherlands Cancer Institute. Tissues were fixed for 24 h in 10% neutral buffered formalin, embedded in paraffin, sectioned at 4 μm and stained with hematoxylin and eosin (H&E). For immunohistochemical analysis, 5 μm paraffin sections were cut, deparaffinized, antigen retrieval was performed, followed by inactivation of endogenous peroxidases by H_2O_2 addition, blocking and primary antibody staining. The following antibodies were used: anti-CD8 (4SM15, eBioscience/ThermoFisher, antigen retrieval: Tris/EDTA, pH 9.0, 1:2000), anti-CD4 14-9766-82, eBioscience/ThermoFisher, antigen retrieval: Tris/EDTA, pH 9.0, 1:1000), anti-Granzyme B (NB100-684, Novus Biologicals, antigen retrieval: Tris/EDTA, pH 9.0, 1:100), anti-phospho-S6 (Ser235/236) (2211, Cell Signaling Technology, antigen retrieval: Tris/EDTA, pH 9.0, 1:400) and Goat-anti-Rabbit-Bio secondary antibody (3052-08, Southern Biotech, 1:100).

Samples were visualized with a BX43 upright microscope (Olympus) and images were acquired using cellSens Entry software (Olympus). Brightness/Contrast for representative images were adjusted equally among groups. Quantitative analysis of cell abundance was performed by counting cells in five 40X fields of view (FOV) of viable tissue per tumor and using the average. For quantification of T cell numbers, peritumoral and intratumoral were assessed separately per tumor. For quantification of necrotic area, H&E images were digitally processed using the Aperio ScanScope (Leica Biosystems) with Aperio Scanscope control

software (version 102.0.0.74) and total tumor area and necrotic area were quantified using ImageJ/FIJI (version 2.0.0).

Statistical analysis

Data analyses were performed using GraphPad Prism (version 8) and Qlucore Omics Explorer (version 3.5). The statistical tests used are described in figure legends. All tests were performed two-tailed. *P*-values < 0.05 were considered statistically significant. Sample sizes for mouse experiments were pre-determined using G*Power software (version 3.1). Heatmaps showing average frequency of immune cell populations in p53 mutant tumors or secreted cytokines were generated using Qlucore Omics Explorer (version 3.5).

Data availability

The ChIP-sequencing data have been deposited in the Gene Expression Omnibus (GEO, NCBI) repository under accession number GSE155639. The enriched proteins of the RIME analysis and mass spectrometry are found in **Supplemental Table 4.1 – 4.5** (available upon request). All further data are available from the authors upon reasonable request.

Acknowledgements

Research in the De Visser laboratory is funded by the Netherlands Organization for Scientific Research (NWO-VICI 91819616), a European Research Council Consolidator award (ERC InflaMet 615300), the Dutch Cancer Society (KWF10083; KWF10623) and Oncode Institute. Research in the Zwart laboratory is funded by the Netherlands Organization for Scientific Research (NWO-VIDI 91716401), the Dutch Cancer Society/Alpe d'HuZes (KWF12018) and Oncode Institute. The proteomics work in this study was supported by the X-omics Initiative, co-funded by the Netherlands Organization for Scientific Research (NWO 184034019). We thank Moshe Oren, Ori Hassin, Giuseppe Mallel and members of the De Visser, Akkari, Jonkers and Kok labs for insightful input. We thank the flow cytometry facility, genomics core facility, animal laboratory facility and animal pathology facility of the Netherlands Cancer Institute for technical assistance.

Contributions

M.D.W. and K.E.d.V. conceived the ideas and designed the experiments. M.D.W. performed experiments and data analysis. S.P., I.M.P, L.H. and W.Z. performed and analyzed ChIP-seq and RIME. O.B.B. and M.A. performed and analyzed mass spectrometry. M.D.W. and K.K. analyzed the immunohistochemistry data. M.D.W., K.K., C.-S.H., E.A.M.R., K.V., D.K., and D.E.M.D. performed animal experiments. A.L. generated KB1P and KP cell lines. K.E.d.V. supervised the study and acquired funding, M.D.W. and K.E.d.V. wrote the paper and prepared the figures with input from all authors.

Conflict of interest statement

W.Z. reports research funding from Astellas Pharma and K.E.d.V. reports research funding from Roche and is consultant for Third Rock Ventures, both outside the scope of this work. The other authors report no competing interests.

Extended Data

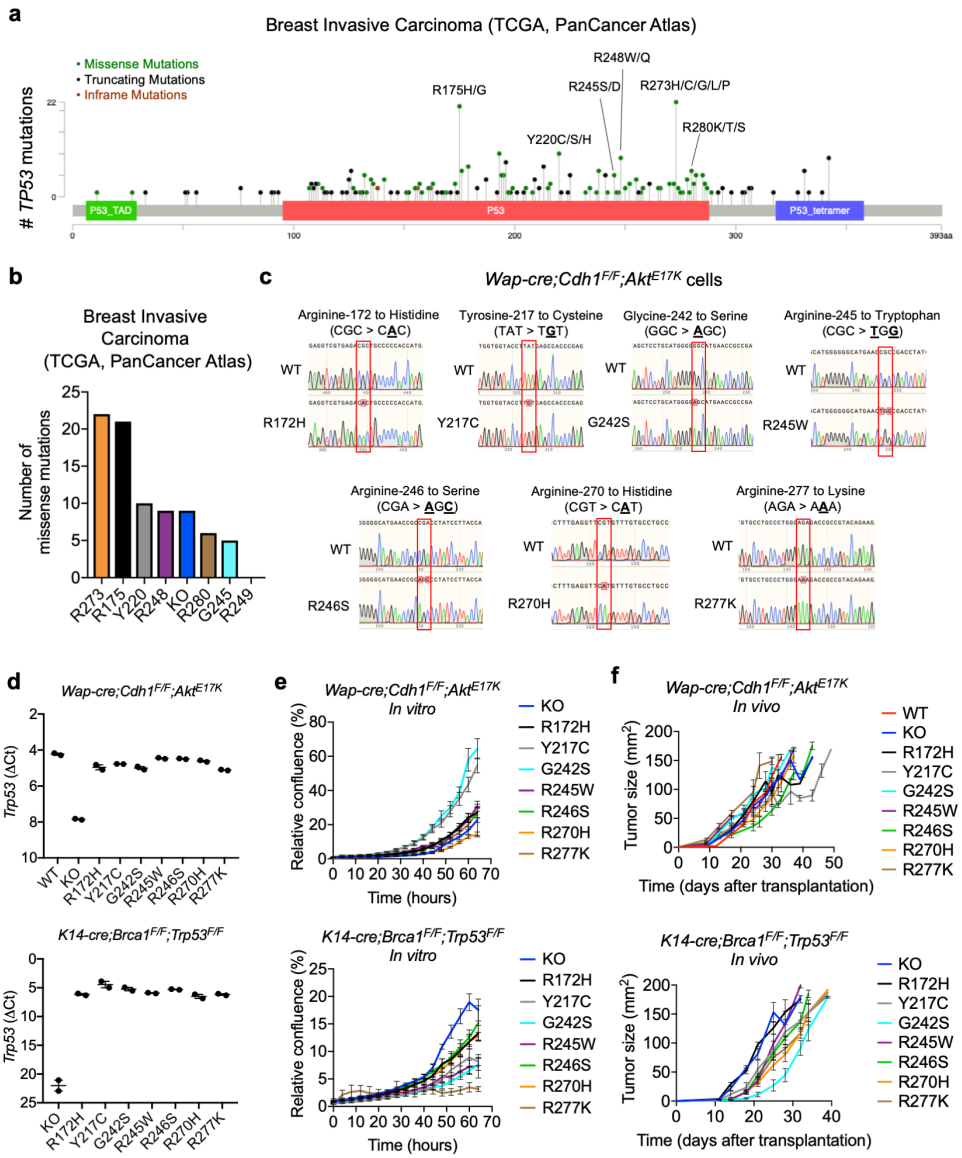

Extended Data Figure 4.1. Prevalence of p53 mutations in human breast cancer and generation of p53 mutant lines. a. Lollipop plot of *TP53* mutations and their prevalence in human breast tumors of the Cancer Genome Atlas (TCGA) Breast Invasive Carcinoma PanCancer Atlas dataset. Mutations used in this study are indicated. Green bar indicates the p53 trans-activation domain. Red bar indicates DNA binding domain. Blue bar indicates tetramerization domain. **b.** Number of samples present in TCGA breast tumors per indicated *TP53* mutant. Homozygous deletion ('Homdel') is considered equivalent to mouse p53-KO. **c.** Sanger sequencing of mutated target regions in the genomic DNA of the mouse *Trp53* gene in *Wap-cre;Cdh1*$^{F/F}$*;Akt*^{E17K} (WEA) cell lines after deletion of endogenous p53 and ectopic expression of mutant p53. WT p53 is shown as reference for each mutation. **d.** RT-qPCR analysis of p53-WT WEA cells and p53-KO and p53-mutant WEA and *K14-cre;Brca1*$^{F/F}$*;Trp53*$^{F/F}$ (KB1P) cell lines (2 replicates/group). KO cells have been transduced with empty vectors (EV). **e.** *In vitro* growth kinetics of WEA and KB1P cells with indicated p53 alterations as measured by IncuCyte (n=5 replicates/group). **f.** *In vivo* growth kinetics of orthotopically transplanted WEA and KB1P tumors with indicated p53 alterations (n=5 mice/group). Data in **d, e** and **f** show mean ± s.e.m.

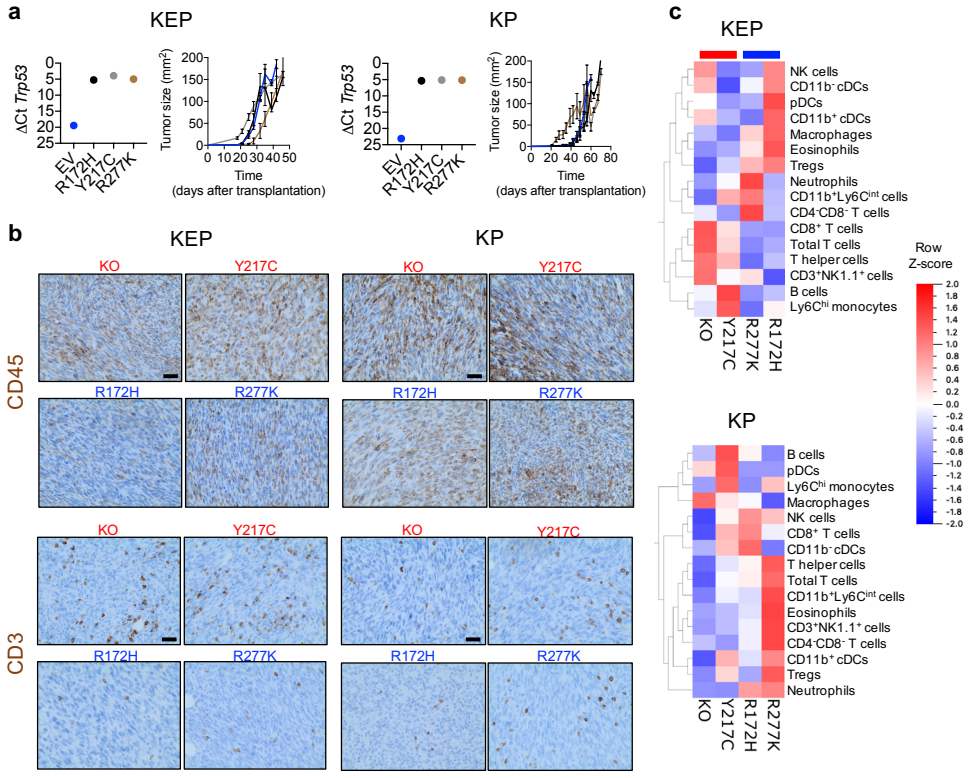

Extended Data Figure 4.2. Immune phenotype in *K14-cre;Cdh1$^{F/F}$;Trp53$^{F/F}$* and *K14-cre;Trp53$^{F/F}$* tumors harboring p53 mutations. a. RT-qPCR analysis of *Trp53* expression after ectopic expression of indicated p53 mutants in KEP and KP cells (average of 2 replicates/group) and tumor growth kinetics after orthotopic transplantation of indicated cells (n=3-5 mice/group for KEP, n=4-5 mice/group for KP). **b.** Representative immunohistochemistry (IHC) images of total immune cell (CD45$^+$) and total T cell (CD3$^+$) levels in KEP and KP tumors with indicated p53 mutations. Bar: 50 μm. **c.** Heatmap of relative immune cell frequencies (% of live cells) in KEP and KP tumors at disease end-stage (tumor size ±225 mm^2). Red and blue bar indicate T cell-inflamed and non-T cell inflamed mutants, respectively (n=3-5 mice/group for KEP, n=4-5 mice/group for KP). Data in **a** show mean ± s.e.m.

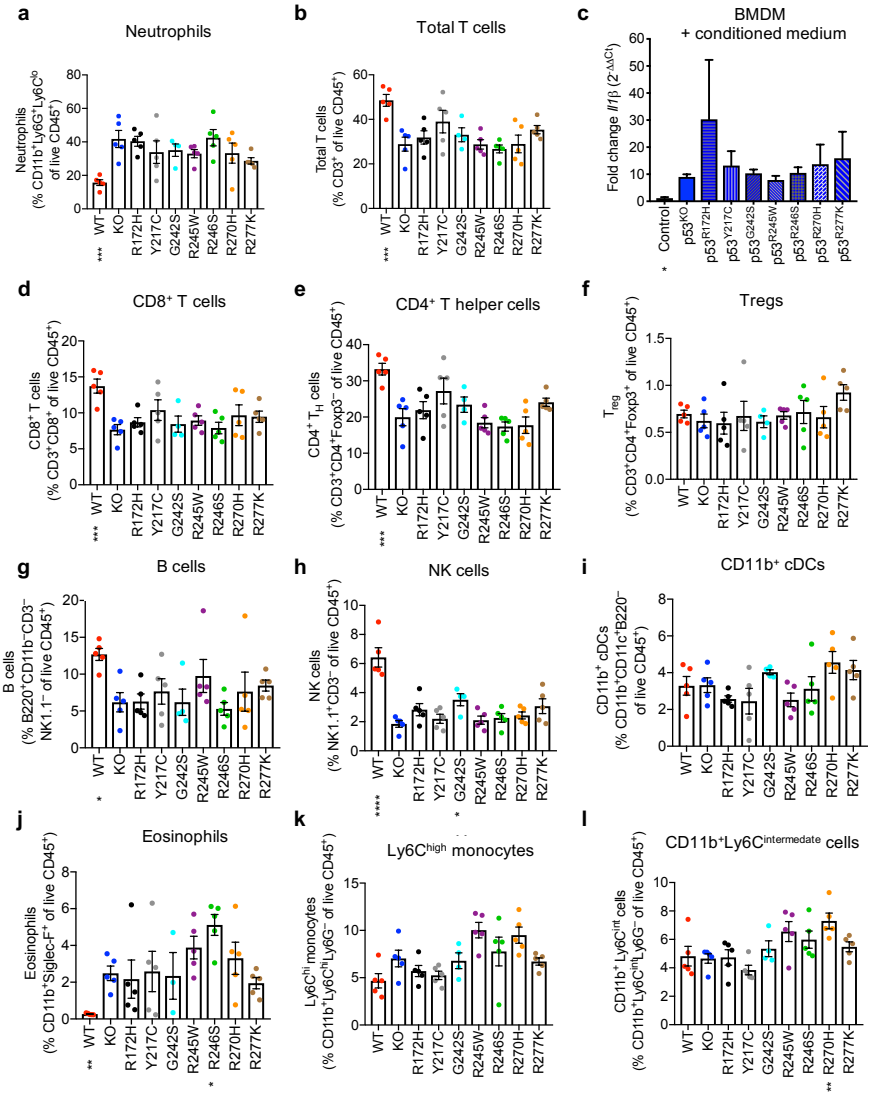

Extended Data Figure 4.3. Systemic inflammation is equally induced by p53 mutant mammary tumors. a. Frequency of circulating neutrophils in mice bearing orthotopically transplanted *Wap-cre;Cdh1$^{F/F}$;Akt^{E17K}* (WEA) tumors with indicated p53 status (n=4-5 mice/group). **b.** Frequency of circulating total T cells (n=4-5 mice/group). **c.** RT-qPCR analysis of *Il-1b* expression in bone marrow-derived macrophages (BMDM) cultured 24 hours with conditioned medium from WEA cells with indicated p53 alterations or control medium (n=4 biological replicates/group in technical duplicate). **d – l.** Frequency of circulating CD8$^+$ T cells (**d**), CD4$^+$FOXP3$^-$ T helper cells (**e**), CD4$^+$FOXP3$^+$ regulatory T cells (Tregs) (**f**), B cells (**g**), Natural Killer (NK) cells (**h**), CD11b$^+$ conventional dendritic cells (cDCs) (**i**), eosinophils (**j**), Ly6C^{high} monocytes (**k**) and CD11b$^+$Ly6C^{intermediate} cells (**l**) (n=4-5 mice/group). Data show mean ± s.e.m. Asterisks indicate statistically significant changes compared to p53-KO group. * $P < 0.05$, ** $P < 0.01$, *** $P < 0.001$, **** $P < 0.0001$, as determined by one-way ANOVA, followed by Tukey's multiple testing correction.

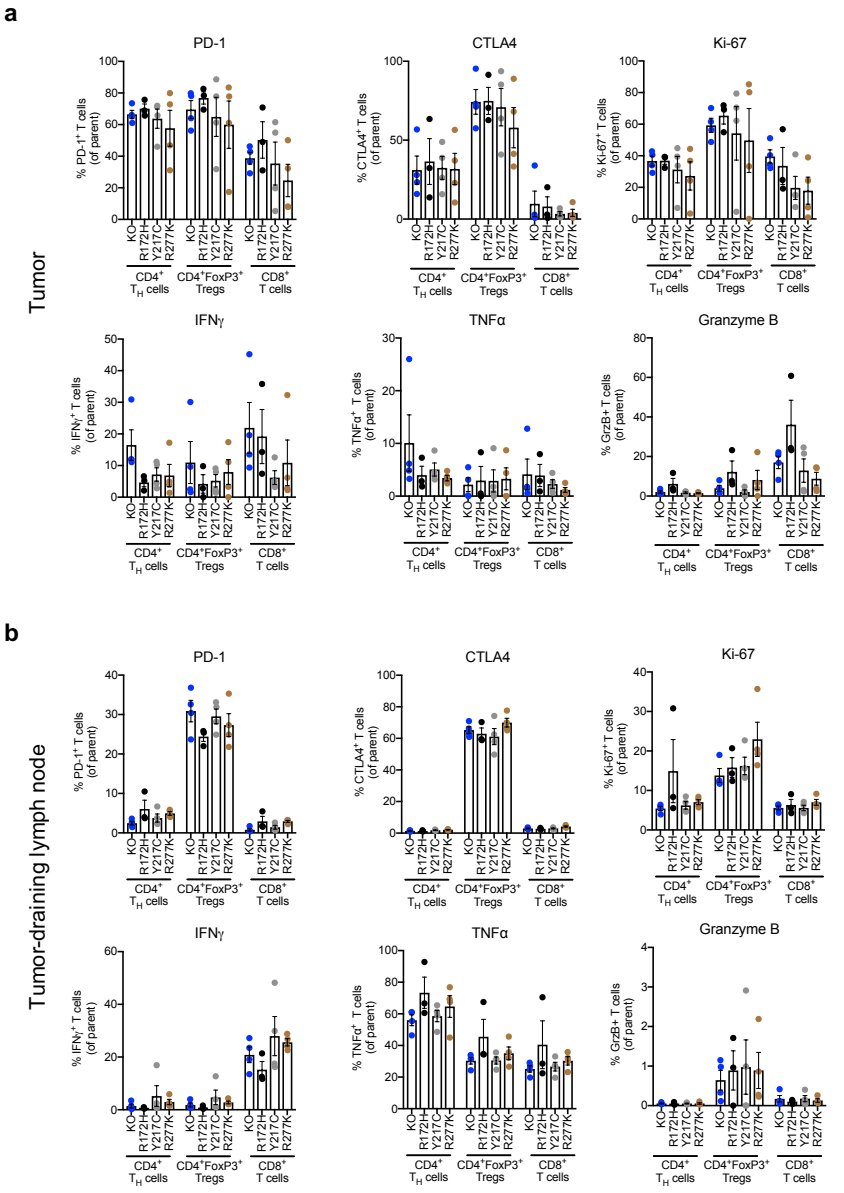

Extended Data Figure 4.4. Ectopic activation of adaptive immune cells elicits equal responses in different p53 mutant tumors. a. Expression of PD-1, CTLA4, Ki-67, IFNγ, TNFα and Granzyme B on intratumoral T_H cells, Tregs and CD8$^+$ T cells of orthotopically transplanted *Wap-cre;Cdh1$^{F/F}$;Akt^{E17K}* (WEA) tumors with indicated p53 mutations, following *ex vivo* stimulation. **b.** Expression of PD-1, CTLA4, Ki-67, IFNγ, TNFα and Granzyme B on T_H cells, Tregs and CD8$^+$ T cells in the tumor-draining (right axillary) lymph node of orthotopically transplanted WEA tumors with indicated p53 mutations, following a 3 hour *ex vivo* stimulation. (n=3-4 mice/group). Data show mean ± s.e.m.

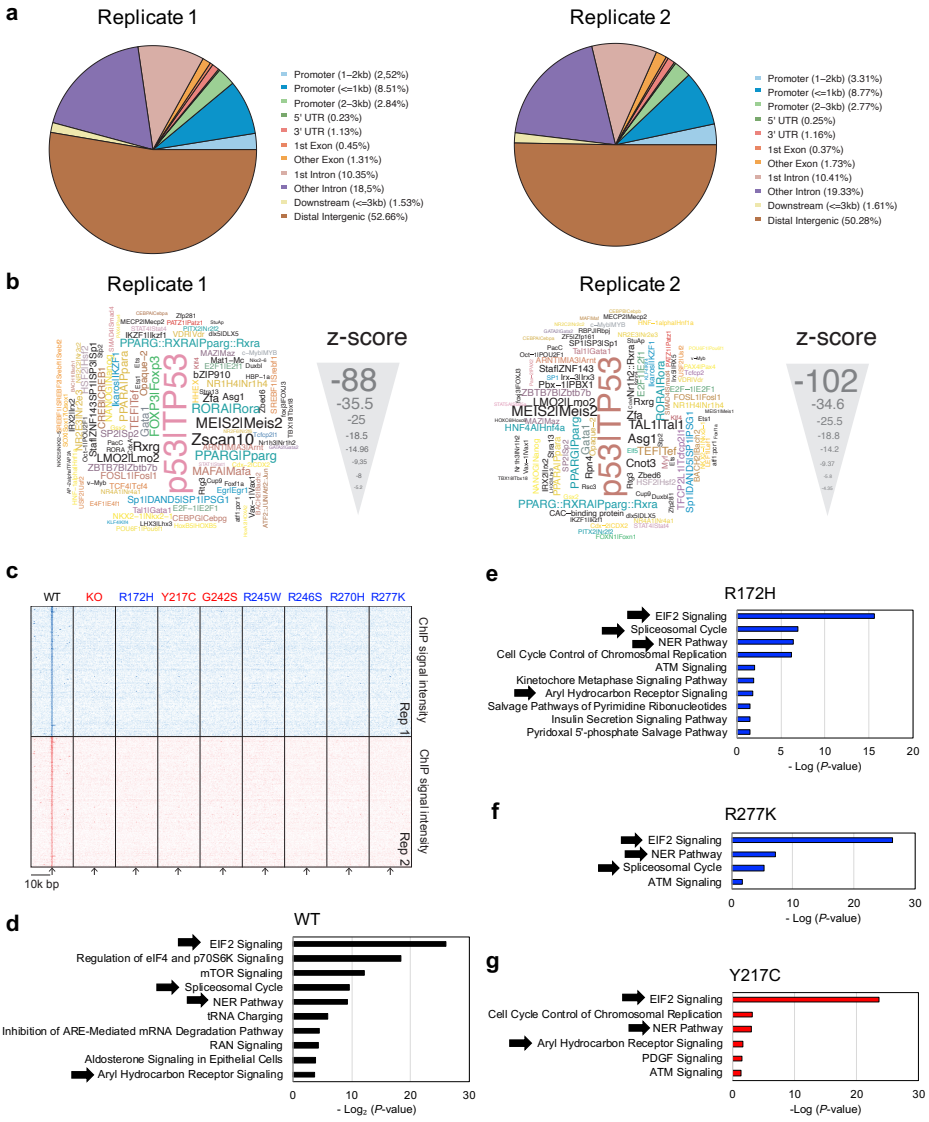

Extended Data Figure 4.5. Chromatin binding properties of WT p53 are lost in all mutant p53 *Wap-cre;Cdh1$^{F/F}$;Akt^{E17K}* cell lines. a. Genomic distributions for the consensus binding sites of p53 in two replicates, as determined by ChIP-seq in *Wap-cre;Cdh1$^{F/F}$;Akt^{E17K}* (WEA) cells. **b.** Predicted binding sites based on sequence motifs in p53 ChIP for two replicates, with negative Z-score of the motifs for binding sites of each factor indicated, showing p53 motifs most significantly enriched. **c.** Heatmap of ChIP-seq signal intensity of called peaks around peak midpoint (arrow) of all WT and mutant p53 WEA cells (n=2 replicates/group), with p53-KO as negative control. **d – g.** Ingenuity Pathway Analysis (IPA) of p53-interacting proteins as determined by RIME showing only significant ($P < 0.05$) signaling pathways with a positive Z-score that are enriched in p53 WT (**d**), p53-R172H (**e**), p53-R277K (**f**) and p53-Y217C (**g**) cells. Black arrows indicate common pathways enriched among all four groups.

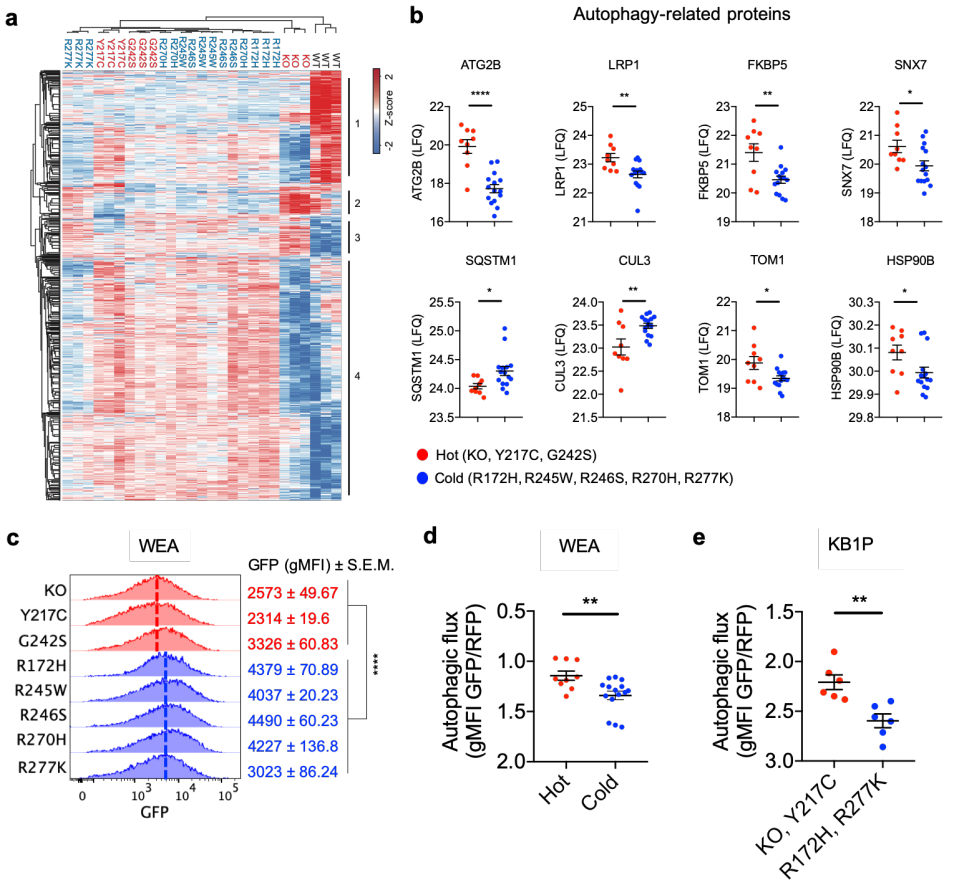

Extended Data Figure 4.6. Autophagy-activating proteins are enriched in T cell inflamed p53 mutants. a. Heatmap depicting unsupervised clustering of differentially expressed proteins (1260 in total) between any of the indicated p53 mutant, KO or WT groups in *Wap-cre;Cdh1$^{F/F}$;Akt^{E17K}* (WEA) cells. Red and blue names of p53 mutants indicate hot and cold phenotypes, respectively (n=3 replicates/group). **b.** Label free quantitation (LFQ) values of autophagy-related proteins in hot (red; KO, Y217C, G242S) or cold (blue; R172H, R245W, R246S, R270H, R277K) p53 mutant WEA cells (n=3 replicates/group). **c.** Representative histograms of GFP-LC3 levels with geometric mean fluorescence intensity (gMFI) annotated for all hot (red; KO, Y217C, G242S) or cold (blue; R172H, R245W, R246S, R270H, R277K) p53 mutant WEA cells transduced with RFP-LC3-GFP (n=3 replicates/mutant). Low GFP indicates high autophagic flux. **d.** Autophagic flux of all p53 mutant WEA cells transduced with RFP-LC3-GFP (n=3 replicates/mutant). **e.** Autophagic flux of all p53 mutant *K14-cre;Brca1$^{F/F}$;Trp53$^{F/F}$* (KB1P) cells transduced with RFP-LC3-GFP (n=3 replicates/mutant).. Data in **b – e** show mean ± s.e.m. Asterisks indicate statistically significant changes. * $P < 0.05$, ** $P < 0.01$, *** $P < 0.001$, **** $P < 0.0001$, as determined by one-way ANOVA, followed by Tukey's multiple testing correction (**b**) or Mann-Whitney U test (**c – e**).

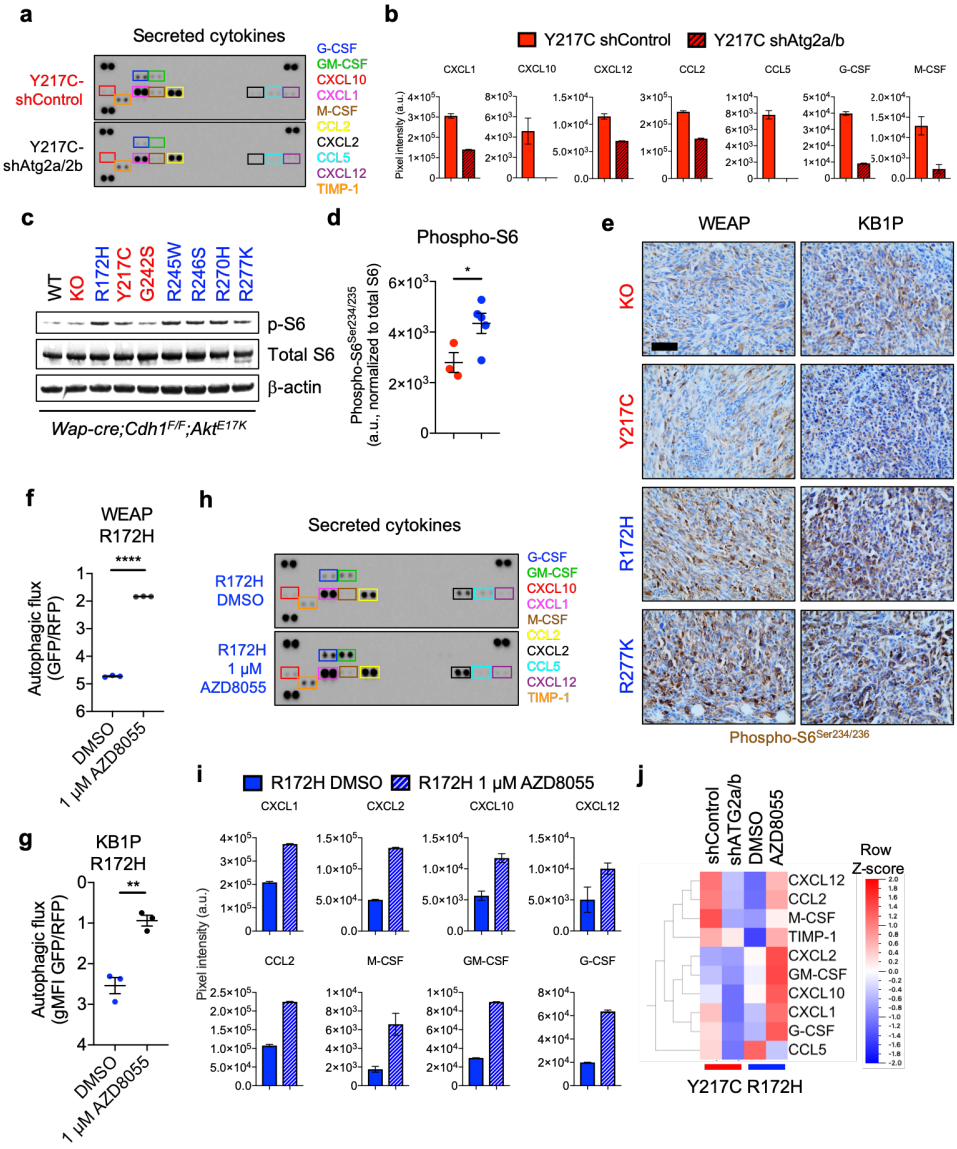

Extended Data Figure 4.7. Disruption of autophagy impairs cytokine secretion by p53^{Y217C} cancer cells, which can be reversed by mTOR inhibition (legend on next page).

Extended Data Figure 4.7. Disruption of autophagy impairs cytokine secretion by p53^{Y217C} cancer cells, which can be reversed by mTOR inhibition. a. Blots of cytokine analysis in conditioned medium (CM) of p53-Y217C WEA cells with *Atg2a/2b* knockdown or control cells. **b.** Average signal intensities of selected secreted cytokines shown in **a** (n=2 replicates/group). **c.** Western blot analysis of mTOR activation (phosphorylated S6) in *Wap-cre;Cdh1$^{F/F}$;Akt^{E17K}* (WEA) cell lines with indicated p53 mutations (red; hot, blue; cold phenotypes). **d.** Quantification of phospho-S6 signal in **c.** Total S6 signal was normalized to loading control β-actin, and phospho-S6 was normalized to normalized total S6 signal. **e.** Representative immunohistochemistry analysis of WEA and *K14-cre;Brca1$^{F/F}$;Trp53$^{F/F}$* (KB1P) tumors with indicated p53 mutations. Bar: 50 μm. **f, g.** Autophagic flux (LC3-GFP/LC3-RFP ratio) of RFP-LC3-GFP transduced p53-R172H mutant WEA (**f**) and KB1P (**g**) cells after overnight exposure to 1 μM mTOR inhibitor AZD8055 or DMSO (n=3 replicates/group). **h.** Blots of cytokine analysis in conditioned medium (CM) of p53-R172H WEA cells after overnight exposure to 1 μM mTOR inhibitor AZD8055 or DMSO. **i.** Average signal intensities of selected secreted cytokines shown in **h** (n=2 replicates/group). **j.** Heatmap depicting quantification of average signal intensities of cytokines detected in CM of WEA cells. Experiments shown in **a, b, h** and **i** were performed simultaneously and blots were exposed at equal length. Data in **b, d, f, g** and **i** show mean ± s.e.m. Asterisks indicate statistically significant changes. * $P < 0.05$, ** $P < 0.01$, **** $P < 0.0001$, as determined by Mann-Whitney U test (**d**) or Student's t-test (**f, g**).

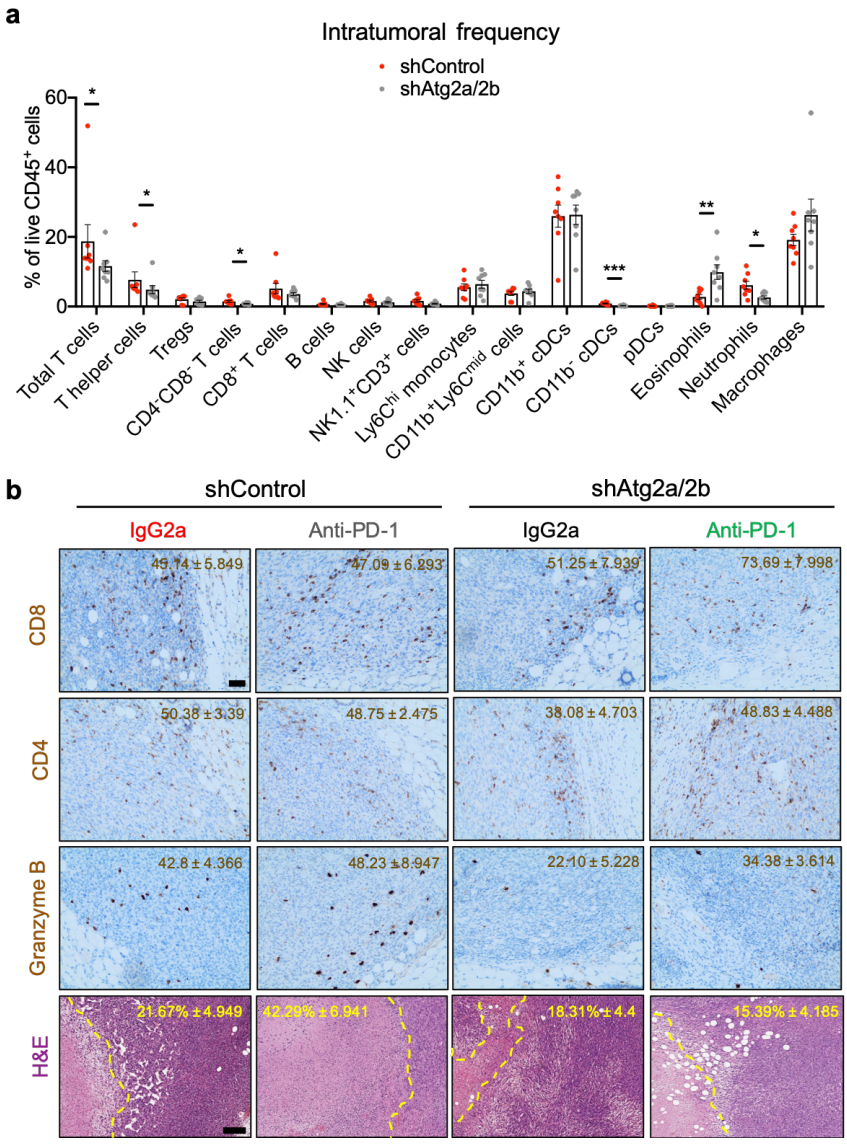

Extended Data Figure 4.8. Silencing of *Atg2a/2b* alters the immune landscape of p53^{Y217C} mutant tumors. a. Flow cytometry analysis of immune landscape of orthotopically transplanted shControl or shAtg2a/2b *Wap-cre;Cdh1$^{F/F}$;Akt^{E17K}* (WEA) p53^{Y217C} tumors at disease end-stage (tumor size ±225 mm^2) (n=8 mice/group). **b.** Representative immunohistochemistry (IHC) images of intratumoral CD4$^+$, CD8$^+$ and Granzyme B$^+$ cells and hematoxylin & eosin (H&E) staining in shControl and shAtg2a/2b p53^{Y217C} WEA tumors at end-stage treated with anti-PD-1 or IgG2a control antibodies. Indicated are intratumoral counts ± s.e.m. for IHC and percentage (%) necrotic area ± s.e.m. for H&E. Yellow line indicates border of necrotic and non-necrotic tumor area. Bar IHC: 50 µm. Bar H&E: 500 µm. Data in **a** and **b** show mean ± s.e.m. Asterisks indicate statistically significant changes. * $P < 0.05$, ** $P < 0.01$, *** $P < 0.001$, as determined by one-way ANOVA (**a**).

Supplemental Information

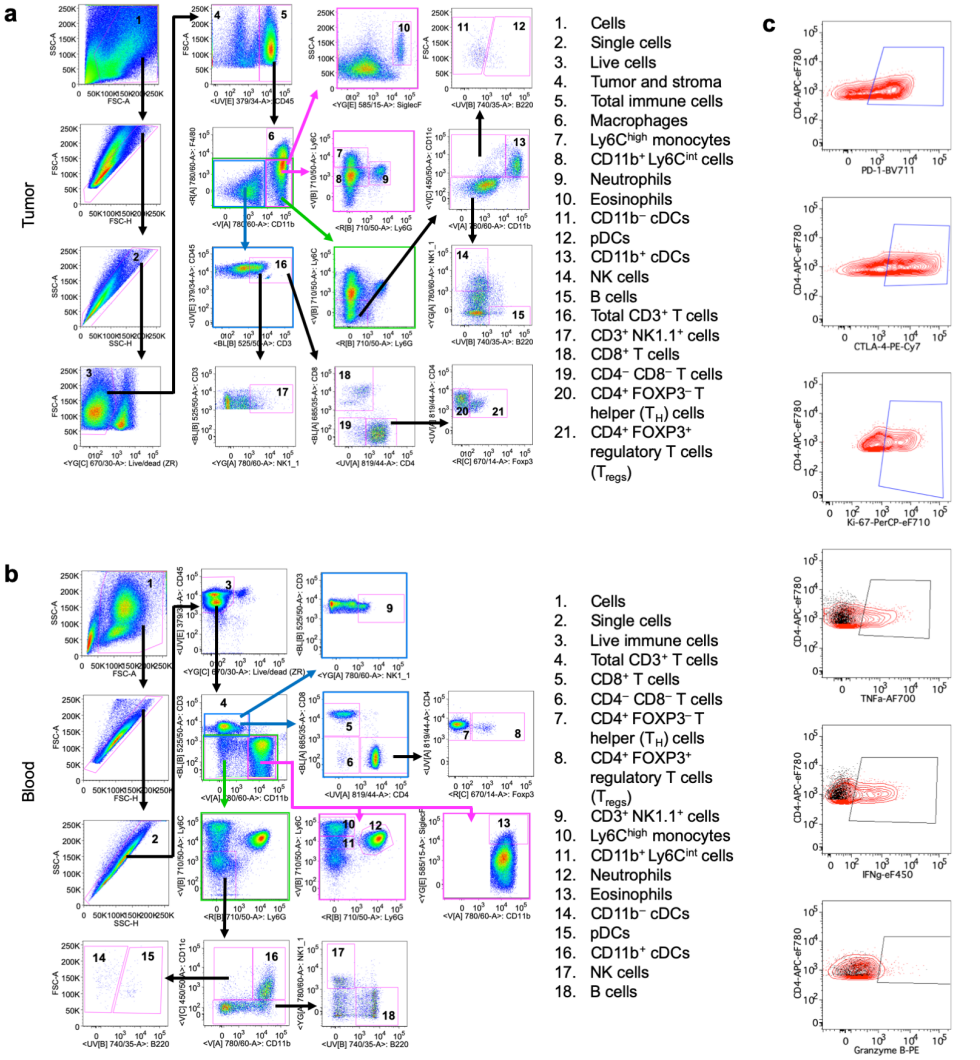

Supplemental Figure 4.1. Gating strategies for immune phenotyping. a. Gating strategy for immune phenotyping in mouse mammary tumors. **b.** Gating strategy for immune phenotyping in blood. **c.** Gating of activation marker and cytokine expression on intratumoral or tumor-draining lymph node T cells. Shown here are representative images for CD4$^+$ FOXP3$^-$ T_H cells. Sample indicated in red is stimulated for 3 hours with PMA, ionononmycin and Golgi-Plug, and sample indicated in black is unstimulated (Golgi-Plug only).

Supplemental tables (available from the author upon request)

Supplemental Table 4.1. List of p53-WT-interacting proteins in *Wap-cre;Cdh1$^{F/F}$;Akt^{E17K}* cells. Label free quantitation difference values of all proteins interacting with p53-WT detected by p53-RIME (n=3 replicates/group). All data was normalized to p53-KO samples.

Supplemental Table 4.2. List of p53-R172H-interacting proteins in *Wap-cre;Cdh1$^{F/F}$;Akt^{E17K}* cells. Label free quantitation difference values of all proteins interacting with p53-R172H detected by p53-RIME (n=4 replicates/group). All data was normalized to p53-KO samples.

Supplemental Table 4.3. List of p53-R277K-interacting proteins in *Wap-cre;Cdh1$^{F/F}$;Akt^{E17K}* cells. Label free quantitation difference values of all proteins interacting with p53-R277K detected by p53-RIME (n=3 replicates/group). All data was normalized to p53-KO samples.

Supplemental Table 4.4. List of p53-Y217C-interacting proteins in *Wap-cre;Cdh1$^{F/F}$;Akt^{E17K}* cells. Label free quantitation difference values of all proteins interacting with p53-R217C detected by p53-RIME (n=4 replicates/group). All data was normalized to p53-KO samples.

Supplemental Table 4.5. Differentially expressed proteins in *Wap-cre;Cdh1$^{F/F}$;Akt^{E17K}* cells with different p53 mutations. Label free quantitation values of all proteins differentially expressed between any of the groups, as assessed by mass spectrometry (n=3 replicates/group).

References

1 Savas, P. *et al.* Clinical relevance of host immunity in breast cancer: from TILs to the clinic. *Nat. Rev. Clin. Oncol.* **13**, 228-241, doi:10.1038/nrclinonc.2015.215 (2016).

2 Emens, L. A. Breast Cancer Immunotherapy: Facts and Hopes. *Clin. Cancer Res.* **24**, 511-520, doi:10.1158/1078-0432.CCR-16-3001 (2018).

3 Stanton, S. E., Adams, S. & Disis, M. L. Variation in the Incidence and Magnitude of Tumor-Infiltrating Lymphocytes in Breast Cancer Subtypes: A Systematic Review. *JAMA Oncol.* **2**, 1354-1360, doi:10.1001/jamaoncol.2016.1061 (2016).

4 Cimino-Mathews, A. *et al.* PD-L1 (B7-H1) expression and the immune tumor microenvironment in primary and metastatic breast carcinomas. *Hum. Pathol.* **47**, 52-63, doi:10.1016/j.humpath.2015.09.003 (2016).

5 Wellenstein, M. D. & de Visser, K. E. Cancer-Cell-Intrinsic Mechanisms Shaping the Tumor Immune Landscape. *Immunity* **48**, 399-416, doi:10.1016/j.immuni.2018.03.004 (2018).

6 Cancer Genome Atlas, N. Comprehensive molecular portraits of human breast tumours. *Nature* **490**, 61-70, doi:10.1038/nature11412 (2012).

7 Kastenhuber, E. R. & Lowe, S. W. Putting p53 in Context. *Cell* **170**, 1062-1078, doi:10.1016/j.cell.2017.08.028 (2017).

8 Schwitalla, S. *et al.* Loss of p53 in enterocytes generates an inflammatory microenvironment enabling invasion and lymph node metastasis of carcinogen-induced colorectal tumors. *Cancer Cell* **23**, 93-106, doi:10.1016/j.ccr.2012.11.014 (2013).

9 Pribluda, A. *et al.* A senescence-inflammatory switch from cancer-inhibitory to cancer-promoting mechanism. *Cancer Cell* **24**, 242-256, doi:10.1016/j.ccr.2013.06.005 (2013).

10 Wörmann, S. M. *et al.* Loss of P53 Function Activates JAK2-STAT3 Signaling to Promote Pancreatic Tumor Growth, Stroma Modification, and Gemcitabine Resistance in Mice and is Associated With Patient Survival. *Gastroenterology* **151**, 180-193, doi:10.1053/j.gastro.2016.03.010 (2016).

11 Blagih, J. *et al.* Cancer-Specific Loss of p53 Leads to a Modulation of Myeloid and T Cell Responses. *Cell Rep.* **30**, 481-496 e486, doi:10.1016/j.celrep.2019.12.028 (2020).

12 Busch, S. E. *et al.* Lung Cancer Subtypes Generate Unique Immune Responses. *J. Immunol.* **197**, 4493-4503, doi:10.4049/jimmunol.1600576 (2016).

13 Stodden, G. R. *et al.* Loss of Cdh1 and Trp53 in the uterus induces chronic inflammation with modification of tumor microenvironment. *Oncogene* **34**, 2471-2482, doi:10.1038/onc.2014.193 (2015).

14 Bezzi, M. *et al.* Diverse genetic-driven immune landscapes dictate tumor progression through distinct mechanisms. *Nat. Med.* **24**, 165-175, doi:10.1038/nm.4463 (2018).

15 Wellenstein, M. D. *et al.* Loss of p53 triggers WNT-dependent systemic inflammation to drive breast cancer metastasis. *Nature* **572**, 538-542, doi:10.1038/s41586-019-1450-6 (2019).

16 Nigro, J. M. *et al.* Mutations in the p53 gene occur in diverse human tumour types. *Nature* **342**, 705-708, doi:10.1038/342705a0 (1989).

17 Hinds, P. W. *et al.* Mutant p53 DNA clones from human colon carcinomas cooperate with ras in transforming primary rat cells: a comparison of the “hot spot” mutant phenotypes. *Cell Growth Differ.* **1**, 571-580 (1990).

18 Baugh, E. H., Ke, H., Levine, A. J., Bonneau, R. A. & Chan, C. S. Why are there hotspot mutations in the TP53 gene in human cancers? *Cell Death Differ.* **25**, 154-160, doi:10.1038/cdd.2017.180 (2018).

19 Muller, P. A. & Vousden, K. H. Mutant p53 in cancer: new functions and therapeutic opportunities. *Cancer Cell* **25**, 304-317, doi:10.1016/j.ccr.2014.01.021 (2014).

20 Dittmer, D. *et al.* Gain of function mutations in p53. *Nat. Genet.* **4**, 42-46, doi:10.1038/ng0593-42 (1993).

21 Olive, K. P. *et al.* Mutant p53 gain of function in two mouse models of Li-Fraumeni syndrome. *Cell* **119**, 847-860, doi:10.1016/j.cell.2004.11.004 (2004).

22 Kotler, E. *et al.* A Systematic p53 Mutation Library Links Differential Functional Impact to Cancer Mutation Pattern and Evolutionary Conservation. *Mol. Cell* **71**, 178-190.e178, doi:10.1016/j.molcel.2018.06.012 (2018).

23 Shahbandi, A., Nguyen, H. D. & Jackson, J. G. TP53 Mutations and Outcomes in Breast Cancer: Reading beyond the Headlines. *Trends Cancer* **6**, 98-110, doi:10.1016/j.trecan.2020.01.007 (2020).

24 Liu, Z. *et al.* TP53 Mutations Promote Immunogenic Activity in Breast Cancer. *J Oncol.* **2019**, 5952836, doi:10.1155/2019/5952836 (2019).

25 Quigley, D. *et al.* Lymphocyte Invasion in IC10/Basal-Like Breast Tumors Is Associated with Wild-Type TP53. *Mol. Cancer Res.* **13**, 493-501, doi:10.1158/1541-7786.MCR-14-0387 (2015).

26 Biton, J. *et al.* TP53, STK11, and EGFR Mutations Predict Tumor Immune Profile and the Response to Anti-PD-1 in Lung Adenocarcinoma. *Clin. Cancer Res.* **24**, 5710-5723, doi:10.1158/1078-0432.CCR-18-0163 (2018).

27 Assoun, S. *et al.* Association of TP53 mutations with response and longer survival under immune checkpoint inhibitors in advanced non-small-cell lung cancer. *Lung Cancer* **132**, 65-71, doi:10.1016/j.lungcan.2019.04.005 (2019).

28 Dong, Z. Y. *et al.* Potential Predictive Value of TP53 and KRAS Mutation Status for Response to PD-1 Blockade Immunotherapy in Lung Adenocarcinoma. *Clin. Cancer Res.* **23**, 3012-3024, doi:10.1158/1078-0432.CCR-16-2554 (2017).

29 Annunziato, S. *et al.* Modeling invasive lobular breast carcinoma by CRISPR/Cas9-mediated somatic genome editing of the mammary gland. *Genes Dev.* **30**, 1470-1480, doi:10.1101/gad.279190.116 (2016).

30 Liu, X. *et al.* Somatic loss of BRCA1 and p53 in mice induces mammary tumors with features of human BRCA1-mutated basal-like breast cancer. *Proc. Natl. Acad. Sci. U. S. A.* **104**, 12111-12116, doi:10.1073/pnas.0702969104 (2007).

31 Walerych, D., Napoli, M., Collavin, L. & Del Sal, G. The rebel angel: mutant p53 as the driving oncogene in breast cancer. *Carcinogenesis* **33**, 2007-2017, doi:10.1093/carcin/bgs232 (2012).

32 Staib, F., Hussain, S. P., Hofseth, L. J., Wang, X. W. & Harris, C. C. TP53 and liver carcinogenesis. *Hum. Mutat.* **21**, 201-216, doi:10.1002/humu.10176 (2003).

33 Derksen, P. W. *et al.* Somatic inactivation of E-cadherin and p53 in mice leads to metastatic lobular mammary carcinoma through induction of anoikis resistance and angiogenesis. *Cancer Cell* **10**, 437-449, doi:10.1016/j.ccr.2006.09.013 (2006).

34 Newman, A. M. *et al.* Robust enumeration of cell subsets from tissue expression profiles. *Nat. Methods* **12**, 453-457, doi:10.1038/nmeth.3337 (2015).

35 Adams, S. *et al.* Pembrolizumab monotherapy for previously untreated, PD-L1-positive, metastatic triple-negative breast cancer: cohort B of the phase II KEYNOTE-086 study. *Ann. Oncol.* **30**, 405-411, doi:10.1093/annonc/mdy518 (2019).

36 Rahnamoun, H. *et al.* Mutant p53 shapes the enhancer landscape of cancer cells in response to chronic immune signaling. *Nat. Commun.* **8**, 754, doi:10.1038/s41467-017-01117-y (2017).

37 Boettcher, S. *et al.* A dominant-negative effect drives selection of TP53 missense mutations in myeloid malignancies. *Science* **365**, 599-604, doi:10.1126/science.aax3649 (2019).

38 Mohammed, H. *et al.* Rapid immunoprecipitation mass spectrometry of endogenous proteins (RIME) for analysis of chromatin complexes. *Nat. Protoc.* **11**, 316-326, doi:10.1038/nprot.2016.020 (2016).

39 Shibutani, S. T., Saitoh, T., Nowag, H., Munz, C. & Yoshimori, T. Autophagy and autophagy-related proteins in the immune system. *Nat. Immunol.* **16**, 1014-1024, doi:10.1038/ni.3273 (2015).

40 Velikkakath, A. K., Nishimura, T., Oita, E., Ishihara, N. & Mizushima, N. Mammalian Atg2 proteins are essential for autophagosome formation and important for regulation of size and distribution of lipid droplets. *Mol. Biol. Cell* **23**, 896-909, doi:10.1091/mbc.E11-09-0785 (2012).

41 Kaizuka, T. *et al.* An Autophagic Flux Probe that Releases an Internal Control. *Mol. Cell* **64**, 835-849, doi:10.1016/j.molcel.2016.09.037 (2016).

42 Kim, Y. C. & Guan, K. L. mTOR: a pharmacologic target for autophagy regulation. *J. Clin. Invest.* **125**, 25-32, doi:10.1172/JCI73939 (2015).

43 Jiang, G. M. *et al.* The relationship between autophagy and the immune system and its applications for tumor immunotherapy. *Mol. Cancer* **18**, 17, doi:10.1186/s12943-019-0944-z (2019).

44 Cordani, M. *et al.* Mutant p53 proteins counteract autophagic mechanism sensitizing cancer cells to mTOR inhibition. *Mol. Oncol.* **10**, 1008-1029, doi:10.1016/j.molonc.2016.04.001 (2016).

45 Oren, M. & Rotter, V. Mutant p53 gain-of-function in cancer. *Cold Spring Harb. Perspect. Biol.*

2, a001107, doi:10.1101/cshperspect.a001107 (2010).
46 Cooks, T. *et al.* Mutant p53 prolongs NF-kappaB activation and promotes chronic inflammation and inflammation-associated colorectal cancer. *Cancer Cell* **23**, 634-646, doi:10.1016/j.ccr.2013.03.022 (2013).
47 Di Minin, G. *et al.* Mutant p53 reprograms TNF signaling in cancer cells through interaction with the tumor suppressor DAB2IP. *Mol. Cell* **56**, 617-629, doi:10.1016/j.molcel.2014.10.013 (2014).
48 Ham, S. W. *et al.* TP53 gain-of-function mutation promotes inflammation in glioblastoma. *Cell Death Differ.* **26**, 409-425, doi:10.1038/s41418-018-0126-3 (2019).
49 Schulz-Heddergott, R. *et al.* Therapeutic Ablation of Gain-of-Function Mutant p53 in Colorectal Cancer Inhibits Stat3-Mediated Tumor Growth and Invasion. *Cancer Cell* **34**, 298-314 e297, doi:10.1016/j.ccell.2018.07.004 (2018).
50 Ghosh, M. *et al.* Mutant p53 suppresses innate immune signaling to promote tumorigenesis. *bioRxiv*, doi:10.1101/2020.03.12.989384 (2020).
51 Wang, S., Jiang, M., Yang, Z., Huang, X. & Li, N. The role of distinct co-mutation patterns with TP53 mutation in immunotherapy for NSCLC. *Genes & Diseases*, doi:10.1016/j.gendis.2020.04.001 (2020).
52 Carlisle, J. W. *et al.* Impact of TP53 mutations on efficacy of PD-1 targeted immunotherapy in non-small cell lung cancer (NSCLC). *J. Clin. Oncol.* **36**, e21090-e21090 (2018).
53 Tasdemir, E. *et al.* Regulation of autophagy by cytoplasmic p53. *Nat. Cell Biol.* **10**, 676-687, doi:10.1038/ncb1730 (2008).
54 Cordani, M., Butera, G., Pacchiana, R. & Donadelli, M. Molecular interplay between mutant p53 proteins and autophagy in cancer cells. *Biochim. Biophys. Acta Rev. Cancer* **1867**, 19-28, doi:10.1016/j.bbcan.2016.11.003 (2017).
55 Choudhury, S., Kolukula, V. K., Preet, A., Albanese, C. & Avantaggiati, M. L. Dissecting the pathways that destabilize mutant p53: the proteasome or autophagy? *Cell Cycle* **12**, 1022-1029, doi:10.4161/cc.24128 (2013).
56 Rosenfeldt, M. T. *et al.* p53 status determines the role of autophagy in pancreatic tumour development. *Nature* **504**, 296-300, doi:10.1038/nature12865 (2013).
57 Zhong, Z., Sanchez-Lopez, E. & Karin, M. Autophagy, Inflammation, and Immunity: A Troika Governing Cancer and Its Treatment. *Cell* **166**, 288-298, doi:10.1016/j.cell.2016.05.051 (2016).
58 Ladoire, S. *et al.* The presence of LC3B puncta and HMGB1 expression in malignant cells correlate with the immune infiltrate in breast cancer. *Autophagy* **12**, 864-875, doi:10.1080/15548627.2016.1154244 (2016).
59 Marsh, T. *et al.* Autophagic Degradation of NBR1 Restricts Metastatic Outgrowth during Mammary Tumor Progression. *Dev. Cell* **52**, 591-604 e596, doi:10.1016/j.devcel.2020.01.025 (2020).
60 Weichhart, T., Hengstschlager, M. & Linke, M. Regulation of innate immune cell function by mTOR. *Nat. Rev. Immunol.* **15**, 599-614, doi:10.1038/nri3901 (2015).
61 Halevy, O., Michalovitz, D. & Oren, M. Different tumor-derived p53 mutants exhibit distinct biological activities. *Science* **250**, 113-116 (1990).
62 Lang, G. A. *et al.* Gain of function of a p53 hot spot mutation in a mouse model of Li-Fraumeni syndrome. *Cell* **119**, 861-872, doi:10.1016/j.cell.2004.11.006 (2004).
63 Cho, Y., Gorina, S., Jeffrey, P. D. & Pavletich, N. P. Crystal structure of a p53 tumor suppressor-DNA complex: understanding tumorigenic mutations. *Science* **265**, 346-355, doi:10.1126/science.8023157 (1994).
64 Joerger, A. C., Ang, H. C. & Fersht, A. R. Structural basis for understanding oncogenic p53 mutations and designing rescue drugs. *Proc. Natl. Acad. Sci. U. S. A.* **103**, 15056-15061, doi:10.1073/pnas.0607286103 (2006).
65 Freed-Pastor, W. A. & Prives, C. Mutant p53: one name, many proteins. *Genes Dev.* **26**, 1268-1286, doi:10.1101/gad.190678.112 (2012).
66 Bellazzo, A., Sicari, D., Valentino, E., Del Sal, G. & Collavin, L. Complexes formed by mutant p53 and their roles in breast cancer. *Breast Cancer (Dove Med Press)* **10**, 101-112, doi:10.2147/BCTT.S145826 (2018).
67 Esteva, F. J., Hubbard-Lucey, V. M., Tang, J. & Pusztai, L. Immunotherapy and targeted therapy combinations in metastatic breast cancer. *Lancet Oncol.* **20**, e175-e186, doi:10.1016/S1470-2045(19)30026-9 (2019).
68 Galluzzi, L., Bravo-San Pedro, J. M., Levine, B., Green, D. R. & Kroemer, G. Pharmacological

modulation of autophagy: therapeutic potential and persisting obstacles. *Nat. Rev. Drug Discov.* **16**, 487-511, doi:10.1038/nrd.2017.22 (2017).
69 Duits, D. E. M., Wellenstein, M. D. & de Visser, K. E. In vitro assessment of cancer cell-induced polarization of macrophages. *Methods Enzymol.* **632**, 133-154, doi:10.1016/bs.mie.2019.06.011 (2020).
70 Sanjana, N. E., Shalem, O. & Zhang, F. Improved vectors and genome-wide libraries for CRISPR screening. *Nat. Methods* **11**, 783-784, doi:10.1038/nmeth.3047 (2014).
71 Brinkman, E. K., Chen, T., Amendola, M. & van Steensel, B. Easy quantitative assessment of genome editing by sequence trace decomposition. *Nucleic Acids Res.* **42**, e168, doi:10.1093/nar/gku936 (2014).
72 Cerami, E. *et al.* The cBio cancer genomics portal: an open platform for exploring multidimensional cancer genomics data. *Cancer Discov.* **2**, 401-404, doi:10.1158/2159-8290.CD-12-0095 (2012).
73 Gao, J. *et al.* Integrative analysis of complex cancer genomics and clinical profiles using the cBioPortal. *Sci. Signal.* **6**, pl1, doi:10.1126/scisignal.2004088 (2013).
74 Mootha, V. K. *et al.* PGC-1alpha-responsive genes involved in oxidative phosphorylation are coordinately downregulated in human diabetes. *Nat. Genet.* **34**, 267-273, doi:10.1038/ng1180 (2003).
75 Subramanian, A. *et al.* Gene set enrichment analysis: a knowledge-based approach for interpreting genome-wide expression profiles. *Proc Natl Acad Sci U S A* **102**, 15545-15550, doi:10.1073/pnas.0506580102 (2005).
76 Liberzon, A. *et al.* The Molecular Signatures Database (MSigDB) hallmark gene set collection. *Cell Syst.* **1**, 417-425, doi:10.1016/j.cels.2015.12.004 (2015).
77 Jersie-Christensen, R. R., Sultan, A. & Olsen, J. V. Simple and Reproducible Sample Preparation for Single-Shot Phosphoproteomics with High Sensitivity. *Methods Mol Biol* **1355**, 251-260, doi:10.1007/978-1-4939-3049-4_17 (2016).
78 Tyanova, S. *et al.* The Perseus computational platform for comprehensive analysis of (prote)omics data. *Nat. Methods* **13**, 731-740, doi:10.1038/nmeth.3901 (2016).
79 Singh, A. A. *et al.* Optimized ChIP-seq method facilitates transcription factor profiling in human tumors. *Life Sci. Alliance* **2**, e201800115, doi:10.26508/lsa.201800115 (2019).
80 Lerdrup, M., Johansen, J. V., Agrawal-Singh, S. & Hansen, K. An interactive environment for agile analysis and visualization of ChIP-sequencing data. *Nat. Struct. Mol. Biol.* **23**, 349-357, doi:10.1038/nsmb.3180 (2016).
81 Stelloo, S. *et al.* Endogenous androgen receptor proteomic profiling reveals genomic subcomplex involved in prostate tumorigenesis. *Oncogene* **37**, 313-322, doi:10.1038/onc.2017.330 (2018).